



# 1 Evaluation of a Coupled Regional Reanalysis for the Mediterranean 2 Region Covering the period 1993-2024

3 Andrea Storto<sup>1,2</sup>, Vincenzo de Toma<sup>1,2</sup>, Chunxue Yang<sup>1,2</sup>

4 <sup>1</sup>Institute of Marine Science (ISMAR), National Research Council (CNR), Rome, I-00133, Rome

5 <sup>2</sup>National Research Center for High Performance Computing, Big Data and Quantum Computing (ICSC), Italy

6 *Correspondence to:* Andrea Storto ([andrea.storto@cnr.it](mailto:andrea.storto@cnr.it)), Chunxue Yang ([chunxue.yang@cnr.it](mailto:chunxue.yang@cnr.it))

7 **Abstract.** Regional reanalyses provide physically consistent reconstructions of past climate, offering a powerful tool for  
8 understanding the processes that shape regional responses to climate change. Here, we introduce MESMAR-R, a newly  
9 developed coupled atmosphere-ocean-hydrology reanalysis for the Mediterranean region. The system couples state-of-the-art  
10 numerical models with data assimilation in both the ocean and the atmosphere, producing a dynamically coherent  
11 reconstruction of the 1993-2024 period. MESMAR-R shows strong performance in the ocean, particularly for sea level, sea-  
12 surface salinity, and upper-layer temperature, confirming its skill in the layers most relevant for air-sea interactions. The  
13 atmospheric component performs reasonably well given its simplified assimilation based on three-dimensional nudging,  
14 yielding basin-scale fields comparable to state-of-the-art reanalyses and maintaining internally consistent coupled air-sea  
15 interactions. Sensitivity experiments show that data assimilation in both the ocean and atmosphere is essential for optimal  
16 performance: coupling alone does not necessarily improve reanalysis skill, but its benefits are relevant for salinity and surface  
17 fluxes and amplify when complemented by data assimilation. The ocean and atmospheric trends reconstructed by MESMAR-  
18 R are physically coherent and consistent with observations, reproducing basin-wide salinification, thermo-halo compensation  
19 in steric sea level, mass-driven sea-level rise, and pronounced near-surface atmospheric warming and drying. MESMAR-R  
20 therefore provides a unique, balanced reconstruction of past Mediterranean climate, suitable for investigating coupled air-sea  
21 processes, compound events, marine extremes, and other phenomena where dynamically consistent atmosphere-ocean  
22 interactions are essential.

23

24 **Short Summary.** The Mediterranean region is one of the fastest-warming areas on Earth, and understanding its changes is  
25 thus crucial. We produced a new reconstruction of the Mediterranean climate for the 1993-2024 period, using a modelling  
26 system that combines weather, ocean, and hydrology information with observations. This new reanalysis offers a clearer picture  
27 of how the region has been warming, drying, and changing over the past 30 years, supporting better studies of extreme events  
28 and climate impacts.

29



## 30 1. Introduction

31 Reanalysis datasets provide temporally and spatially continuous representations of the Earth system, or any of its components,  
32 by combining numerical model simulations with historical observations through data assimilation techniques (e.g., Storto et  
33 al., 2019a). These datasets are essential for climate monitoring, model validation, and understanding past climate variability.  
34 While global reanalyses, such as ERA5 (Hersbach et al., 2020) and MERRA-2 (Gelaro et al., 2017) in the atmosphere or GREP  
35 (Storto et al., 2019b) in the ocean, offer broad coverage, their limited horizontal resolution may hinder their ability to accurately  
36 represent mesoscale processes, especially in regions with complex geography such as the Mediterranean, which is the focus  
37 of the present study. The Mediterranean basin is widely recognized as a climate change hotspot, experiencing rates of warming  
38 exceeding the global average and undergoing rapid changes in hydro-climatic extremes (Cramer et al., 2018; Lionello and  
39 Scarascia, 2018). Projected increases in temperature, decreases in precipitation, and enhanced variability in oceanographic and  
40 atmospheric conditions pose serious challenges for ecosystems, water resources, and human activities across the region.

41 In contrast to global products, high-resolution regional climate models (RCMs) have been developed to dynamically downscale  
42 global reanalyses and provide a refined depiction of climate processes at local to regional scales (e.g., Ruti et al., 2016). These  
43 regional reanalyses are particularly important in areas with significant land-sea contrasts, steep topography, and densely  
44 populated coastal zones, where the impact of climate extremes can be severe (e.g., Senatore et al., 2020; Fox-Hughes et al.,  
45 2022).

46 The importance of regional reanalyses is testified by their increasing development and adoption. The Copernicus Marine  
47 Service provides a Mediterranean ocean reanalysis (e.g., Escudier et al., 2021), while the Copernicus Climate Service has  
48 developed European-scale regional atmospheric reanalyses (e.g., CERRA; Ridal et al., 2024). However, to date, most available  
49 products are either uncoupled or limited to single components: ocean-only or atmosphere-only. Furthermore, some downscaled  
50 reanalyses lack any form of data assimilation, limiting their utility for monitoring and decision-making. Regional coupled  
51 reanalyses over the Mediterranean Sea are expected to become critically important for climate services and downstream  
52 applications because they provide a physically consistent, high-resolution reconstruction of the complex air-sea-land  
53 interactions, enabling improved assessment of marine heatwaves (e.g., Camus et al., 2021), storm surge and coastal flooding  
54 risks (e.g., Juza et al., 2022), which directly support sectors like fisheries management, renewable energy planning, and coastal  
55 adaptation strategies (e.g., Soukissian et al., 2021). Furthermore, regional coupled reanalyses will be increasingly vital for  
56 training deep-learning emulators (Doury et al., 2023) because they offer high-resolution, physically consistent input-output  
57 datasets that capture air-sea-land feedback, enabling efficient and accurate surrogate modeling of regional climate processes  
58 for applications such as bias correction, super-resolution downscaling, and rapid scenario exploration (e.g., van der Meer et  
59 al., 2023).

60 Coupled reanalysis systems, which combine ocean and atmosphere models with concurrent assimilation, offer a more  
61 physically consistent reconstruction of the Earth system by representing feedback across components. While global coupled  
62 reanalyses such as CERA-20C (Laloyaux et al., 2018) have demonstrated the value of this approach, no such product has been  
63 available at the regional scale for the Mediterranean. Recent studies highlight the potential of coupled regional systems to  
64 improve the representation of events like medicanes (Storto et al., 2023).

65 To fill this gap, we present a new high-resolution regional coupled reanalysis for the Mediterranean Sea over the period 1993-  
66 2024. The system is based on the MESMAR coupled model configuration (Storto et al., 2023), which integrates the WRF  
67 atmospheric model and the NEMO ocean model, with interactive river runoff and land surface modelling components. Ocean  
68 data assimilation is implemented via a 3D variational (3DVAR) scheme, while the atmosphere is constrained at the large scale,



69 through spectral nudging, toward ERA5. The configuration thus ensures that large-scale consistency with global reanalyses is  
70 preserved while allowing the model to resolve regional-scale features (Storto et al., 2023). The system assimilates in-situ and  
71 satellite observations in the ocean, providing a dynamically consistent estimate of the Mediterranean climate state across the  
72 atmosphere and ocean components.

73 This paper introduces the dataset (section 2) and presents a first evaluation against many observational datasets (in section 3).  
74 Additionally, comparisons with existing regional and global reanalyses provided by Copernicus Marine and Climate Services  
75 are included for selected metrics, together with an analysis of sensitivity experiments (section 4) and key climatic trends  
76 (section 5). The coupled nature of this reanalysis and the inclusion of data assimilation in both ocean and atmosphere represent  
77 a significant advancement in regional Earth system reanalyses for the Mediterranean region.

## 78 **2. Data and Methods**

### 79 **2.1 Earth System Model configuration**

80 The MESMAR modeling system couples three components: an atmosphere (WRF), ocean (NEMO), and hydrology (HD)  
81 models, via the OASIS3-MCT coupler, and it is described in detail in Storto et al. (2023). The atmospheric core is WRF  
82 (v4.3.3, Skamarock et al., 2021), implemented over the Euro-Mediterranean domain (~15 km horizontal grid, 41 hybrid  
83 vertical levels). WRF is a non-hydrostatic model with a 60-second timestep. Physics options include Thompson microphysics,  
84 RRTMG radiation, the Noah-MP land surface model (4 soil layers), the Mellor-Yamada (Nakanishi and Niino 2006), PBL  
85 closure, and the Grell-Freitas cumulus scheme for subgrid convection. Lateral atmospheric forcing is provided via a 10-point  
86 sponge layer relaxing toward three-hourly ERA5 reanalysis fields (Hersbach et al., 2020).

87 The ocean component is NEMO (v4.0.7, Madec et al., 2017) covering the Mediterranean (Atlantic box to Dardanelles) on a  
88 regular ~7 km grid with 72 vertical levels (with partial steps at bottom). The NEMO baroclinic timestep is 450s, while the  
89 barotropic timestep is 6s, with the split-explicit free-surface formulation. Shortwave radiation follows a three-band scheme  
90 (Morel and Maritorena, 2001) using monthly satellite chlorophyll data (Brewin et al., 2015). Horizontal mixing uses a  
91 Laplacian diffusion (viscosity via bi-Laplacian) with coefficients ~80 m<sup>2</sup>/s ( $4.5 \times 10^9$  m<sup>4</sup>/s<sup>3</sup>), increased by 20% near Gibraltar  
92 and the Aegean. Vertical mixing is handled by a General Length Scale (GLS) scheme (Mellor-Yamada, 1982; closure with  
93 Canuto et al., 2001, stability). Ocean boundaries are forced by the ECMWF ORAS5 reanalysis (Zuo et al., 2019) with Flather  
94 barotropic conditions and prescribed baroclinic velocities, and a 10-point relaxation of temperature and salinity toward ORAS5  
95 fields. River discharge from the HD model is injected at coastlines; the Black Sea (Dardanelles) outflow uses climatology  
96 (Kourafalou & Barbopoulos, 2003).

97 Interactive rivers are provided by the hydrological discharge model (HD v5.1, Hagemann et al., 2020). HD is based on the  
98 MPI hydrology scheme (MPI-HM; Hagemann & Dümenil Gates, 2001) with specialized developments for coupling. It runs at  
99 0.5° resolution over Europe, with a 30-minute timestep. To improve stability, HD implements a conservative smoothing of  
100 river outflow: each discharge is spread to a 5×5 grid around the target ocean point. HD collects surface and subsurface runoff  
101 from WRF, and routes it to NEMO coastal points via the coupler.

102 The coupling between the models is handled by OASIS3-MCT (v5.0, Craig et al., 2017). All exchanged fields are mapped  
103 with first-order conservative interpolation, at 30-minute intervals. Key coupling variables include surface fluxes of momentum,  
104 heat, and freshwater (computed in WRF using the Janjić surface scheme), sea surface temperature (SST) and salinity (SSS)  
105 from NEMO, surface pressure from WRF (for inverse-barometer correction), and river discharge from HD to NEMO. Thus,



106 air-sea fluxes are generated in the atmosphere and passed to the ocean, while SST and currents and atmospheric pressure  
107 influence the atmosphere and ocean, respectively, and runoff links hydrology and ocean.

## 108 **2.2 Data assimilation**

109 MESMAR-R employs a weakly coupled data assimilation system. The ocean uses a 3DVAR scheme (Storto et al., 2018)  
110 updated every 3 days. Background-error covariances are derived from multi-year monthly mean anomalies with respect to the  
111 long-term climatology (1998-2021), from a previous iteration of the coupled reanalysis. Observations include subsurface  
112 profiles (XBT, CTD, moored instruments, Argo/glider floats) from the UK Met Office EN4 dataset (Good et al., 2013), with  
113 variational quality control enabled (Storto, 2016), and along-track altimetry data from CMEMS (Pujol et al., 2023), assimilated  
114 with a dynamic height observation operator (Storto et al., 2011) and the latest Mediterranean Sea Mean Dynamic Topography  
115 (MDT) from the Copernicus Marine Service (Jousset et al., 2025). A weak surface analysis is applied via relaxation of SST  
116 and SSS toward reference analyses (CNR-ISMAR SST and EN4 SSS), with e-folding times of ~15 days (SST) and 300 days  
117 (SSS). Additionally, a large-scale bias correction scheme, as in Storto and Yang (2024), is applied to minimize drifts in the  
118 deep ocean layers.

119 Atmospheric assimilation is achieved by spectral nudging in the WRF model. Large-scale (synoptic) components of wind,  
120 temperature, and humidity are continuously relaxed toward three-hourly ECMWF ERA5 fields. Scales longer than ~850 km  
121 (wavenumbers  $\leq 6$  zonally and  $\leq 5$  meridionally) are constrained, with nudging timescales of order 1 h for winds and  
122 temperature, and 1 day for humidity. This approach maintains large-scale consistency with the ERA5 reanalysis (Hersbach et  
123 al., 2020) while allowing mesoscale features to develop freely (in both the atmosphere and the ocean, like medicanes, see  
124 Storto et al., 2013).

## 125 **2.3 Changes with respect to the pilot version**

126 The MESMAR-R reanalysis is an improved version compared to a first, unpublished, iteration (covering the period 1998-  
127 2022), with a few upgrades that mostly concern the ocean component. Besides the temporal extension, the present version now  
128 includes i) the assimilation of altimetry data in the ocean data assimilation system; ii) a different set of background-error  
129 covariances, calculated from the long-term mean anomalies of the previous reanalysis iteration, thus better representing the  
130 error structures of the coupled reanalysis and leading to better verification skill scores; iii) a deep-ocean large-scale bias  
131 correction scheme. Additionally, the NEMO model now uses XIOS 2.5 for input/output operations, permitting a more flexible  
132 choice of ocean output fields.

## 133 **2.4 Experiments**

134 In addition to the nominal reanalysis setup (MESMAR-R), covering the 32 years from 1993 to 2024, we have also performed  
135 a few other sensitivity experiments, mostly devoted to understanding the relative impact of data assimilation and coupling for  
136 the enhancement of the reanalysis skill scores and key processes, with emphasis on the ocean component of the coupled  
137 reanalysis. Experiments are summarized below, and are all run for the shorter period from 2000 to 2020.

138 We performed a set of experiments switching on/off the data assimilation in both components and the coupling to the  
139 atmosphere. Such a set allows us to disentangle the effects of ocean or atmosphere data assimilation and the coupling, on key  
140 oceanic skill scores and metrics that will be introduced in section 4.

141



<i>NAME</i>	<i>Atm</i>	<i>Oce</i>	<i>Purpose</i>	<i>Period</i>
<b>MESMAR-R</b>	Data Assimilation	Data Assimilation	Coupled Reanalysis	1993-2024
<b>COA</b>	Simulation	Data Assimilation	Impact of atmospheric data assimilation	2000-2020
<b>COS</b>	Simulation	Simulation	Coupled Simulation	2000-2020
<b>UOS</b>	Not present	Simulation	Forced ocean Simulation	2000-2020
<b>UOA</b>	Not present	Data Assimilation	Forced ocean Reanalysis	2000-2020

142 **Table 1. List of reanalysis experiments performed. *Simulation* means that no data assimilation is employed.**

143

144 **2.4 Verification data and methods**

145 Several datasets were used for verifying the reanalysis against. We used in particular:

146 i) gridded sea surface temperature, salinity, and sea level (absolute dynamic topography, ADT) data from the Copernicus  
 147 Marine Service (L4 ADT, Ballarotta et al., 2013, from which also EKE is calculated; L4 SST, Pisano et al., 2020; L4 SSS,  
 148 Sammartino et al., 2022);

149 ii) in-situ profiles extracted from the UK MetOffice EN4 dataset (Good et al., 2013);

150 iii) e-OBS gridded near-surface atmospheric variables from the Copernicus Climate Change Service (Haylock et al.,  
 151 2008);

152 iv) Mixed layer depth (MLD) data from the SeaDataCloud (SDC\_MED\_DP1);

153 v) ocean heat content from the Copernicus Marine Service Ocean Monitor Indicator (von Schuckmann et al., 2018);

154 vi) precipitation over ocean from the Global Precipitation Climatology Project (GPCP, Adler et al., 2003).

155 Some of these datasets are not independent, strictly speaking, as they are assimilated into the system. However, we use lower-  
 156 frequency based metrics for SST, SSH, and SLA (monthly means), while for in-situ profiles, statistics are computed from  
 157 innovation data before the assimilation of the observations. RMSEs in section 3 are calculated from the daily mean fields; for  
 158 altimetry, given the fact that each product may use different MDT, the long-term mean SSH from each experiment is  
 159 subtracted, meaning in facts that RMSE corresponds to the standard deviation of the innovations.

160 As reference datasets to compare skill score metrics, we used the Mediterranean Sea ocean reanalysis MEDREA24 (Escudier  
 161 et al., 2021) and the Mercator Ocean International global ocean reanalysis GLORYS12 (Lellouche et al., 2021) for the ocean  
 162 component, and the ECMWF ERA5 reanalysis (Hersbach et al., 2020) and CERRA (Ridal et al., 2024) for the atmosphere.  
 163 All these reanalyses represent state-of-the-science systems, either with global or regional focus. Climate diagnostics presented  
 164 later mostly consist of linear trends over the full period. Total trends are calculated from the monthly mean data. Additionally,  
 165 for ocean diagnostics, we subdivide the Mediterranean Sea into the western Mediterranean Sea (WMED) and the eastern  
 166 Mediterranean Sea (EMED), divided by a straight line across the Strait of Sicily (at 37°N from Tunisia to Sicily).

167 **3. Validation**

168 In this section, we revise basic validation metrics from the MESMAR-R reanalysis and compare them with reference reanalysis  
 169 datasets, introduced in section 2.4, for comparison. Table 2 shows the RMSE for ocean parameters (temperature and salinity  
 170 for different depth ranges, and sea surface temperature, salinity, and height), over the 2000-2020 period.



171 The MESMAR-R reanalysis shows particularly strong skill at the sea surface. Compared with the regional MEDREA24 and  
 172 the global GLORYS12, it delivers the lowest RMSE for sea surface height, with values slightly better than GLORYS12 and  
 173 markedly better than MEDREA24. Similarly, MESMAR-R clearly outperforms both competitors in sea surface salinity, where  
 174 the error is reduced by more than half compared with GLORYS12. For sea surface temperature, MESMAR-R is nearly  
 175 indistinguishable from MEDREA24, both substantially outperforming GLORYS12. These results highlight the robustness of  
 176 the coupled reanalysis in capturing surface variability, which is critical for mesoscale dynamics, air-sea fluxes, and the  
 177 freshwater balance of the Mediterranean.

178 In the upper ocean, MESMAR-R maintains a strong performance. Temperature in the 20–60 m layer shows the lowest RMSE  
 179 among all products, while at 0–20 m the skill is essentially comparable to MEDREA24 and better than GLORYS12. Salinity  
 180 in the upper 210 m is well represented, too, with MESMAR-R either leading or effectively tied for the best performance.  
 181 Below this depth, however, MEDREA24 generally has a slight advantage, particularly for temperatures between 60 and 400  
 182 m, where MESMAR-R exhibits higher errors than both the regional and global products. At deeper layers (400-1000 m),  
 183 differences among the three systems are small, and MESMAR-R typically places second behind MEDREA24 but ahead of  
 184 GLORYS12.

185 Looking at profiles of bias (Figure 1), all three reanalyses show a small fresh bias in the upper layers, most pronounced in the  
 186 top 50 m, but MESMAR-R (blue) exhibits the smallest amplitude at the sea surface. Below about 100 m, all products converge  
 187 toward near-zero bias. For temperature, the three systems exhibit a weak warm bias near the surface that decreases with depth.  
 188 MESMAR-R shows a bias magnitude comparable to or slightly smaller than MEDREA24 above 100 m, and both regional  
 189 reanalyses outperform GLORYS12, which displays a more persistent warm bias extending deeper into the thermocline. Below  
 190 200 m, MESMAR-R’s bias remains very close to zero, suggesting good thermal consistency with in-situ observations and  
 191 minimal drift at depth.

192

<i>Metric</i>	<i>MESMAR-R</i>	<i>MEDREA24</i>	<i>GLORYS12</i>
<b>S0-20   T0-20 (psu   °C)</b>	0.222   1.189	0.254   1.175	0.367   1.227
<b>S20-60   T20-60 (psu   °C)</b>	0.209   1.087	0.228   1.131	0.229   1.208
<b>S60-210   T60-210 (psu   °C)</b>	0.113   0.417	0.114   0.358	0.123   0.402
<b>S210-400   T210-400 (psu   °C)</b>	0.054   0.261	0.048   0.210	0.055   0.240
<b>S400-600   T400-600 (psu   °C)</b>	0.037   0.173	0.033   0.145	0.041   0.186
<b>S600-1000   T600-1000 (psu   °C)</b>	0.027   0.104	0.025   0.091	0.028   0.105
<b>SST (°C)</b>	0.342	0.331	0.490
<b>SSS (psu)</b>	0.314	0.331	0.784
<b>SSH (cm)</b>	3.4	5.3	3.5

193 **Table 2. Root mean square error for the ocean, in comparison with other state-of-the-art reanalyses. The parameters**  
 194 **include temperature (T, in °C) and salinity (S, in psu), sea surface temperature (SST, in °C), sea surface salinity (SSS,**  
 195 **in psu), and sea surface height (SSH, in m). The calculation covers the period 2000-2020.**

196

197 The spatial distribution of RMSE (Figure 2) confirms the overall strengths of MESMAR-R, while also highlighting regional  
 198 differences. For sea surface temperature (SST), the absolute RMSE map shows widespread errors below 0.5 °C across most



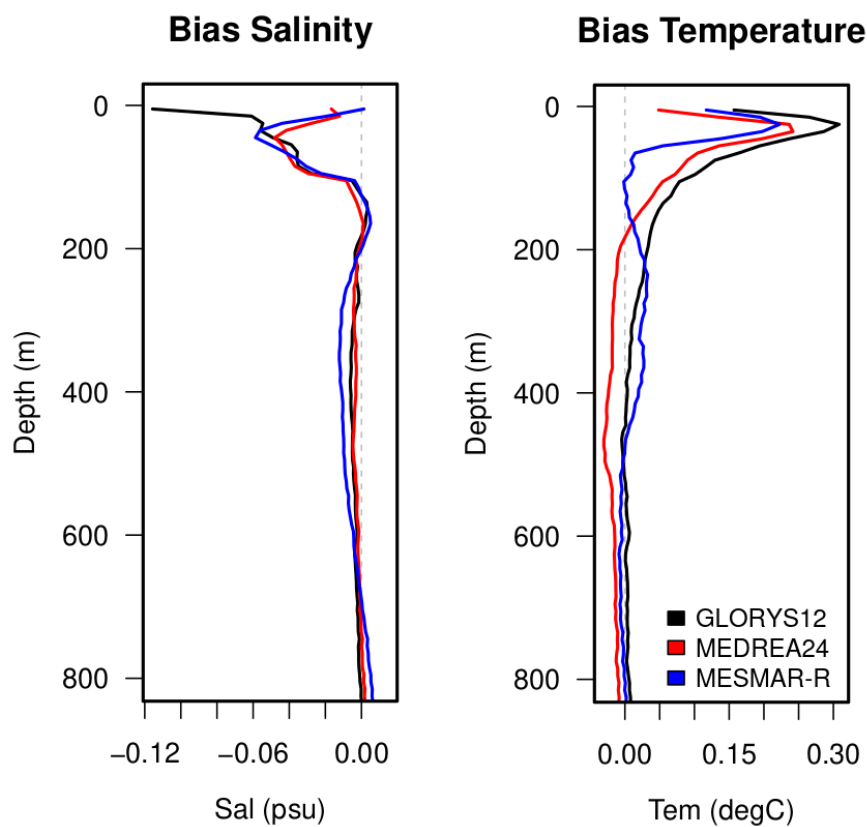
199 of the basin, with slightly elevated values along the northern Adriatic and Aegean Seas, and locally in the western basin. The  
200 difference plots (middle and right panels of Figure 2) indicate that MESMAR-R generally performs as good as MEDREA24,  
201 with small areas of improvement in the Levantine Basin and central Mediterranean, but slightly higher errors along parts of  
202 the western basin and, locally, elsewhere. In contrast, MESMAR-R systematically outperforms GLORYS12 almost  
203 everywhere, with particularly marked improvements in the Adriatic and Aegean Sea, the Levantine Basin, and the Alboran  
204 Sea.

205 For sea surface salinity (SSS), MESMAR-R achieves basin-wide errors below 0.5 psu except for localized peaks in the northern  
206 Aegean. Compared with MEDREA24, there are uniform and widespread improvements, with peaks near the Po river mouth  
207 and local deterioration in proximity to the Dardanelles, likely amplified by differences in the boundary conditions therein.  
208 Against GLORYS12, MESMAR-R demonstrates a clear gain almost everywhere, with the largest improvements in the  
209 northern Adriatic and Aegean seas, likely driven by the better river discharge specification than in the global reanalysis.

210 The sea surface height (SSH) comparison is especially promising, as MESMAR-R exhibits low RMSE values across the entire  
211 basin, typically under 0.04 m. The difference maps confirm that MESMAR-R consistently outperforms MEDREA24  
212 throughout the Mediterranean, with the most pronounced improvements in the western basin and Levantine Sea. Compared  
213 with GLORYS12, MESMAR-R shows a systematic advantage in the eastern Mediterranean, while locally GLORYS12 tends  
214 to outperform MESMAR-R.

215

216



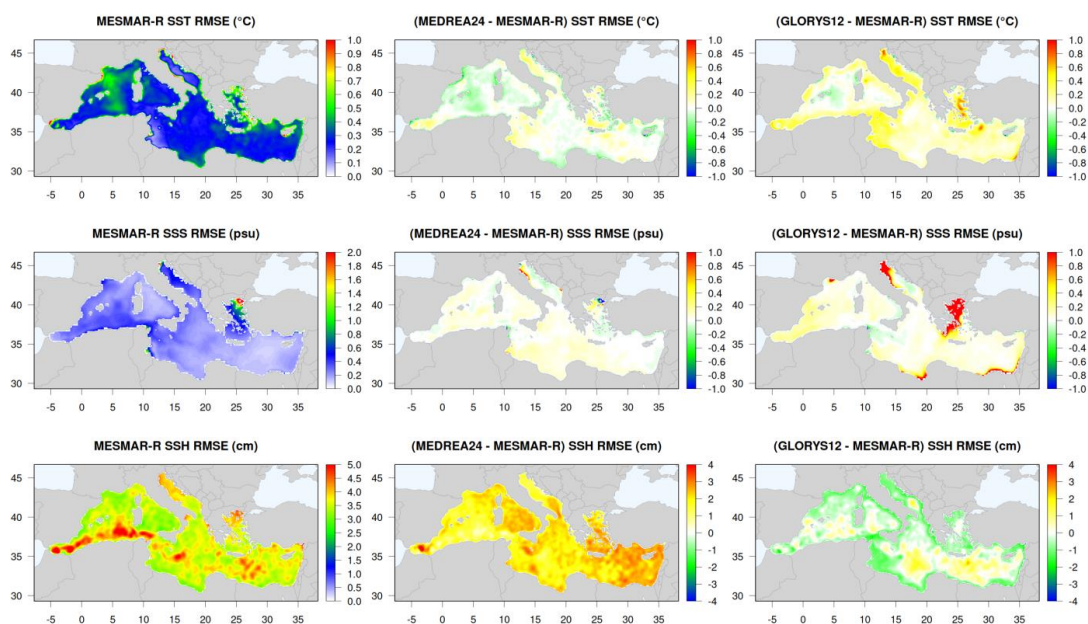
217

218 **Figure 1. Profiles of salinity (left panel) and temperature (right panel) bias, calculated against all available in-situ**  
219 **profiles, for MESMAR-R in comparison with other state-of-the-art reanalyses. The calculation covers the period 2000-**  
220 **2020, and the bias is defined as model minus observations.**

221

222

223



224

225 **Figure 2. Maps of RMSE against sea surface observations (SST in °C, SSS in psu, and SSH in cm), in comparison with**  
226 **other state-of-the-art reanalyses. Left panels show the MESMAR-R RMSE, while middle and right panels show the**  
227 **RMSE difference between either MEDREA24 or GLORYS12 and MESMAR-R (where positive, MESMAR-R provides**  
228 **the smallest RMSE). The calculation covers the period 2000-2020.**

229

230

231



232

<i>Metric</i>	<i>MESMAR-R</i>	<i>ERA5</i>	<i>CERRA</i>
<b>T2M (°C)</b>	1.38	1.24	1.14
<b>RH2M (%)</b>	7.63	7.26	6.61
<b>MSLP (hPa)</b>	2.61	2.35	2.38
<b>WS10M (m s<sup>-1</sup>)</b>	0.91	0.64	0.67
<b>PRECIP-LAND (mm/day)</b>	1.37	0.89	-
<b>PRECIP-OCE (mm/day)</b>	1.17	1.06	-

233 **Table 3. Root mean square error for selected atmospheric parameters, in comparison with other state-of-the-art**  
 234 **reanalyses. T2M: 2m air temperature; RH2M: 2m relative humidity; MSLP: mean sea level pressure; WS10M: wind**  
 235 **speed at 10m; PRECIP: total precipitation (either over land or ocean).**

236

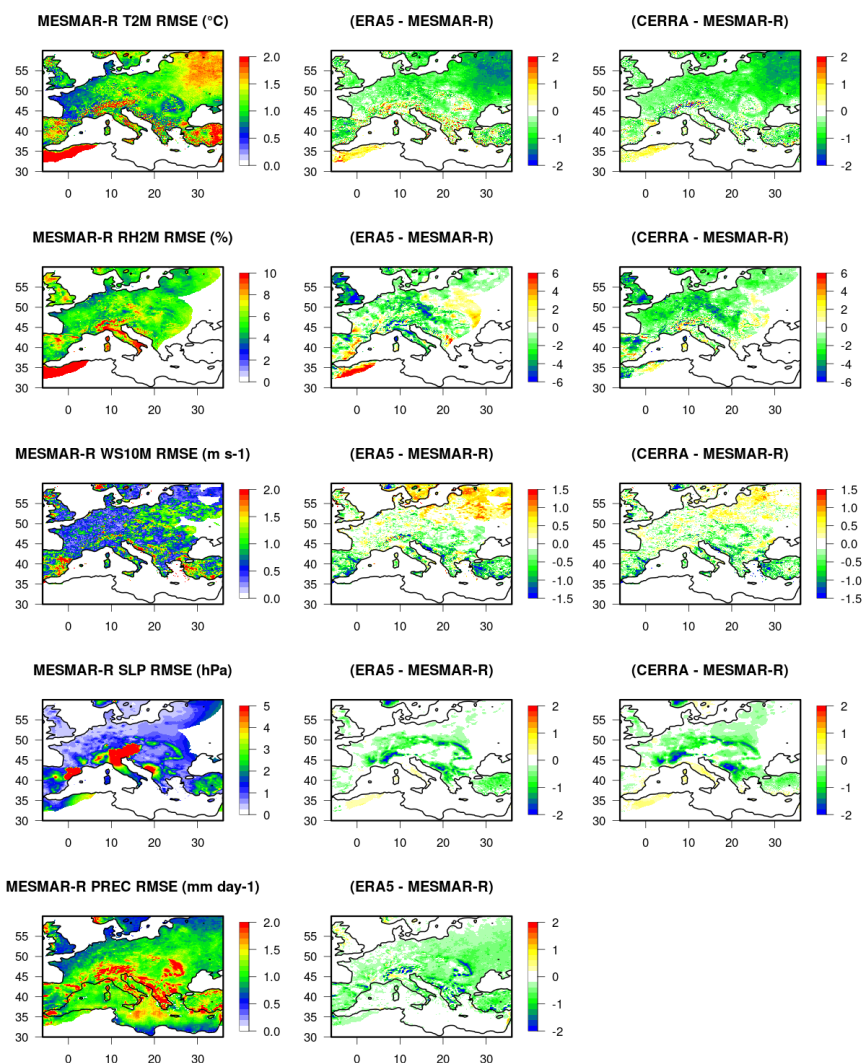
237 Moving to atmospheric parameter validation, area-averaged scores show MESMAR-R generally has slightly higher RMSE  
 238 than ERA5 or CERRA for near-surface variables (Table 3, see the caption therein for the abbreviation of parameters): T2M  
 239 (1.38 °C vs 1.24/1.14), RH2M (7.63% vs 7.26/6.61), WS10M (0.91 m s<sup>-1</sup> vs 0.64/0.67), and MSLP (2.61 hPa vs 2.35/2.38).  
 240 For precipitation, the gap is larger over land (1.37 vs 0.89 mm day<sup>-1</sup> to ERA5) and modest over ocean (1.17 vs 1.06 mm day<sup>-1</sup>),  
 241 where evaluation uses GPCP. MESMAR-R is worse overall but still within the same order of magnitude as the state-of-the-art  
 242 reanalyses.

243 The maps and RMSE-difference panels, in Figure 3, confirm this picture. For all variables, most of the domain shows  
 244 ERA5/CERRA with equal or lower RMSE than MESMAR-R (negative differences), but MESMAR-R achieves localized  
 245 improvements (positive differences) in pockets tied to complex coastlines and orography (e.g., coastal belts and island regions)  
 246 and over a few marine areas where sharp air–sea fluxes may prevail. For T2M and RH2M, small coastal patches show  
 247 MESMAR-R advantages. A large cold bias near Siberian affects the skill scores for MESMAR-R in the eastern part of the  
 248 domain, due to suboptimal land model performances therein (Storto et al., 2023); for WS10M, the northern part of the domain  
 249 and scattered marine areas exhibit marginal gains; MSLP shows very narrow bands in the southernmost part of the MESMAR  
 250 domain, where MESMAR-R reduces error relative to ERA5/CERRA; and for precipitation, ERA5 provides the best skill scores  
 251 almost everywhere. Taken together, the maps indicate MESMAR-R worsens most of the time, but can outperform locally,  
 252 typically in small, dynamically or observationally challenging sub-regions.

253 MESMAR-R’s atmospheric skills are generally worse yet broadly comparable to ERA5/CERRA, which is consistent with  
 254 expectations given MESMAR-R’s very simple atmospheric data-assimilation scheme. The localized wins suggest that targeted  
 255 refinements (e.g., boundary-layer/precipitation physics or enhanced atmospheric DA) could close much of the remaining gap  
 256 without altering the ocean-focused design goals.

257

258



259

260 **Figure 3. Maps of RMSE against atmospheric near-surface gridded observations (T2M in °C, RH2M in %**  
261 **m s<sup>-1</sup>, SLP in hPa, and PREC in mm day<sup>-1</sup>), in comparison with other state-of-the-art reanalyses. Left panels show the**  
262 **MESMAR-R RMSE, while middle and right panels show the RMSE difference between either ERA5 or CERRA and**  
263 **MESMAR-R (where positive, MESMAR-R provides the smallest RMSE). The calculation covers the period 2000–2020.**

264

265

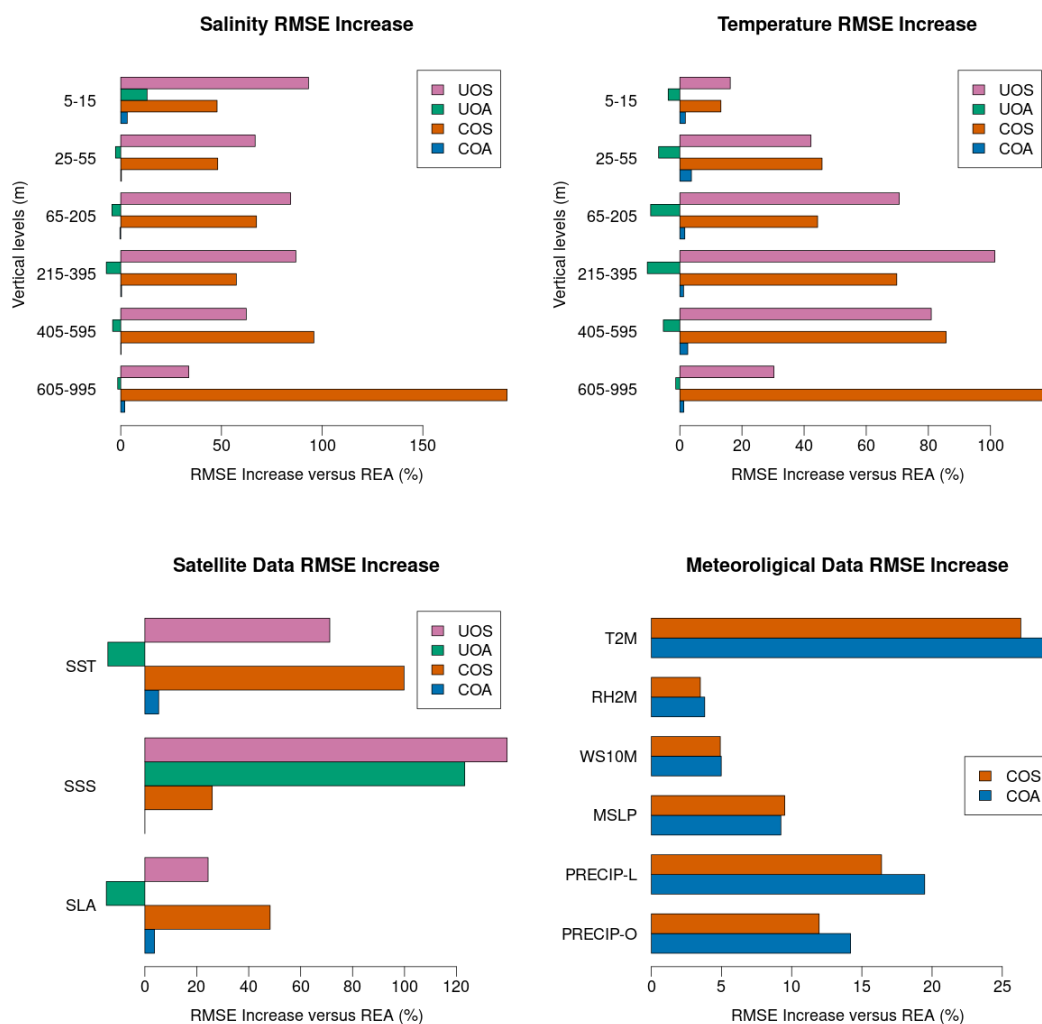
266



267 **4. Sensitivity to coupling and data assimilation**

268 In this section, we compare the MESMAR-R reanalysis with the sensitivity experiments described in section 2.4, to assess the  
 269 relative merits of data assimilation and interactive coupling in the MESMAR-R performances. This section includes both a  
 270 comparison of skill scores and key oceanic processes.

271



272

273 **Figure 4. RMSE increase (in %) compared to MESMAR-R for the experiments described in Table 1, for several oceanic**  
 274 **and atmospheric parameters.**

275 The sensitivity experiments confirm the expected hierarchy among configurations in the comparison of RMSE (see the RMSE  
 276 increase bar plots in Figure 4). The fully coupled free simulation (COS) consistently shows the largest RMSE increases,



277 particularly at depth, indicating that the absence of any data assimilation in coupled mode leads to a rapid degradation of the  
278 subsurface structure. In contrast, the uncoupled ocean simulation (UOS) performs better than COS but is still significantly  
279 worse than MESMAR-R, reflecting the stabilizing influence of the ERA5 atmospheric forcing, which effectively acts as a  
280 weak atmospheric constraint. Interestingly, for some parameters (most notably sea surface salinity (SSS) and upper-ocean  
281 salinity), the coupling provides a measurable improvement, suggesting that the explicit exchange of freshwater fluxes helps  
282 preserve a more realistic surface salinity balance. This may also be due to the different bulk formulas employed in the coupled  
283 configuration compared to the NEMO uncoupled setup, although it is not technically possible to disentangle the two changes.

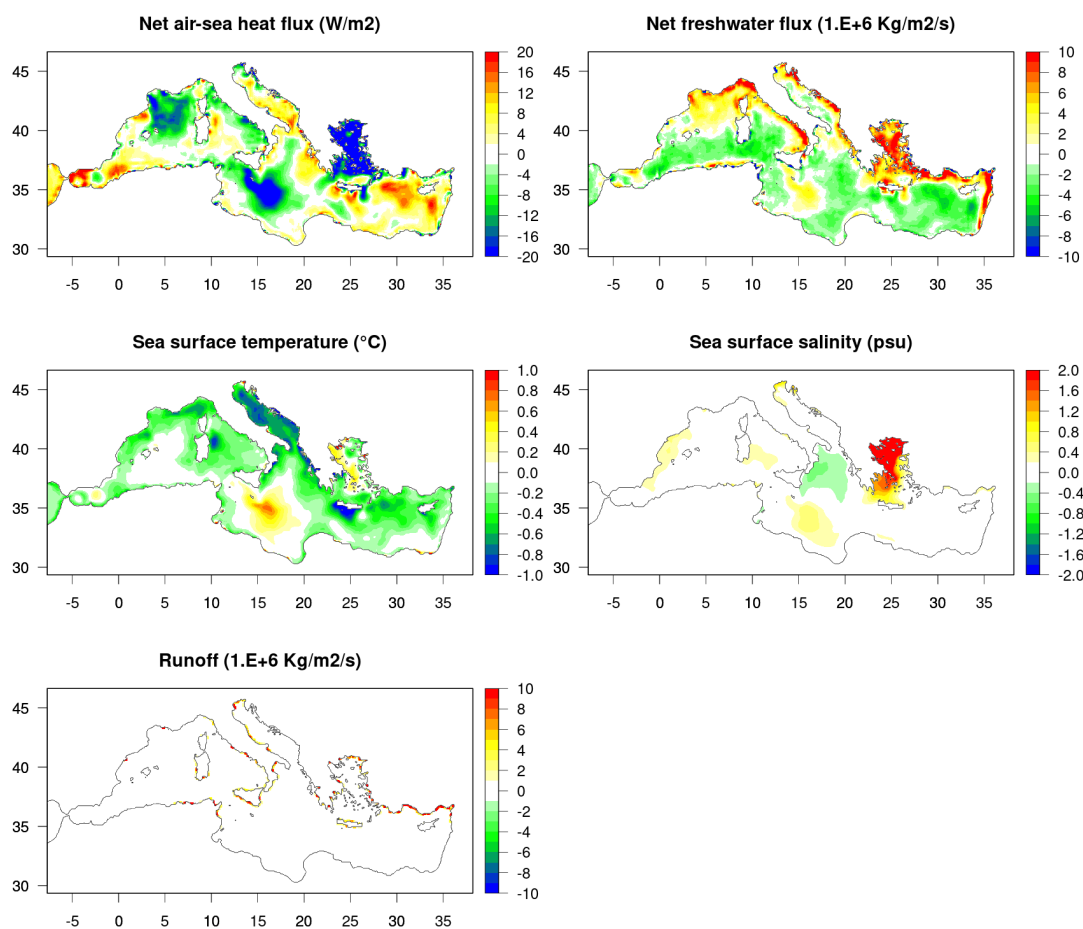
284 The uncoupled ocean reanalysis (UOA) exhibits slight overall improvements compared with MESMAR-R, except for SSS and  
285 salinity in-situ verification in the top 15m, where the coupled configuration performs marginally better, as explained earlier.  
286 This outcome indicates that the combination of ocean data assimilation and prescribed atmospheric reanalysis forcing tends to  
287 outperform the coupled system when coupling errors outweigh flux benefits, except for metrics directly linked to freshwater  
288 closure. Conversely, the coupled ocean analysis (COA), which retains ocean data assimilation but excludes atmospheric  
289 assimilation, shows small but statistically significant degradations in a few key parameters, namely temperature near the base  
290 of the mixed layer, sea level anomaly (SLA), and sea surface temperature (SST). These changes imply that the atmospheric  
291 data assimilation employed in MESMAR-R exerts a positive influence on the air–sea interface, improving consistency in  
292 surface heat and momentum fluxes.

293 The verification against meteorological observations (Figure 4, bottom right panel) reveals moderate RMSE increases for both  
294 coupled configurations (COS and COA) compared with the full reanalysis. The largest degradation occurs for near-surface air  
295 temperature (T2M), where RMSE increases exceed 20%, followed by precipitation, particularly over land (PRECIP-L), where  
296 errors rise by about 15–20%. In contrast, relative humidity (RH2M) and 10 m wind speed (WS10M) show only minor increases  
297 of a few percent, while mean sea level pressure (MSLP) exhibits intermediate sensitivity (around 10%). Notably, COS  
298 generally performs slightly better than COA for several parameters, especially T2M and precipitation, suggesting that the  
299 inclusion of ocean data assimilation in COA may introduce small imbalances at the air–sea interface, which in turn degrade  
300 the consistency of near-surface atmospheric fields. These results indicate that, while the overall atmospheric performance of  
301 both coupled configurations remains broadly comparable, the interaction between ocean assimilation and the coupled fluxes  
302 can generate small spurious surface adjustments, underscoring the delicate balance required to maintain physical coherence in  
303 coupled data assimilation systems. In any case, atmospheric data assimilation, albeit simple, provides important benefits to the  
304 atmospheric performance of the coupled reanalysis.

305 The surface flux differences (Figure 5) between the coupled (COS) and uncoupled (UOS) simulations highlight the physical  
306 mechanisms through which coupling alters SST and SSS, and they are broadly consistent with the performance differences  
307 documented in the sensitivity experiments. In the Aegean Sea, and to a lesser extent in the area south of Sicily, the signal is  
308 particularly clear: the net heat flux difference is negative (reduced downward heat flux), while the net freshwater flux (upward)  
309 difference is positive, indicating enhanced evaporation. Together, these patterns point to stronger latent heat loss in COS,  
310 which cools the surface and simultaneously increases salinity through evaporative concentration. This mechanism aligns well  
311 with the SSS RMSE improvement observed for COS in this region and explains the localized SST differences. In other regions,  
312 the coupling influence is more heterogeneous. Along the Alboran and Levantine basins, patches of increased downward heat  
313 flux coincide with small reductions in evaporation, suggesting coupling-induced adjustments in wind speed and humidity that  
314 alter the surface energy balance without producing a uniform SST or SSS response. The runoff anomalies shown in the bottom  
315 panel are spatially limited and generally small but mostly positive, implying that river-input differences may not be the  
316 dominant drivers of basin-wide changes but can affect locally the salinity variations.



317



318

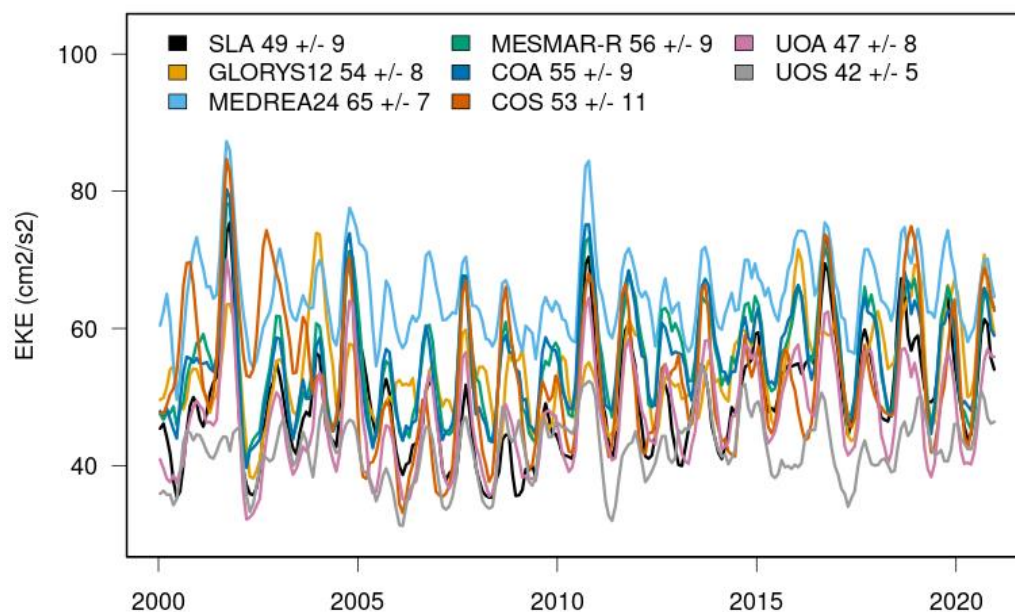
319 **Figure 5. Long-term averaged (2000-2020) air-sea flux and surface parameter differences between the COS and UOS**  
320 **sensitivity experiments (namely, showcasing the impact of the interactive coupling with WRF). Following the NEMO**  
321 **convention, net air-sea heat flux is downward, while net freshwater flux is upward.**

322

323



### Eddy Kinetic Energy (from SSH)



324

325 **Figure 6. Eddy kinetic energy (EKE) timeseries, calculated from the MESMAR-R reanalysis, gridded altimetry data,**  
326 **the MEDREA24 and GLORYS12, and the sensitivity experiments, over the period 2000-2020. For all datasets, EKE is**  
327 **calculated from sea level, adopting the usual geostrophic relationship to calculate geostrophic currents.**

328

329 Next, we review the impact of the different configurations on mesoscale eddy activity, ocean heat content, and deep-water  
330 formation. Eddy Kinetic Energy (EKE), computed from SSH under the geostrophic assumption for all datasets for the sake of  
331 consistency, reveals distinct dynamical signatures across the experiments (see Figure 6 for EKE timeseries in the  
332 Mediterranean Sea, and Figure 7 for EKE maps and differences). MESMAR-R exhibits consistently elevated EKE, both in the  
333 spatial maps and the basin-averaged time series, indicating that both data assimilation and coupling actively energize the  
334 mesoscale. Its values fall reasonably close to the observational benchmark derived from L4 altimetric sea-level anomalies  
335 (SLA), with the main discrepancy appearing near the Strait of Gibraltar, where strong tides, steep topography, and intense  
336 barotropic flows may amplify representation errors in either observations or the model. In contrast, MEDREA24 shows EKE  
337 values that are substantially higher than all other systems, consistently with its much finer horizontal resolution ( $1/24^\circ$ ), which  
338 can resolve smaller eddies and sharper gradients that naturally increase EKE. The spatial patterns suggest that MESMAR-R  
339 differs most strongly from SLA and GLORYS12 in parts of the southern Mediterranean.

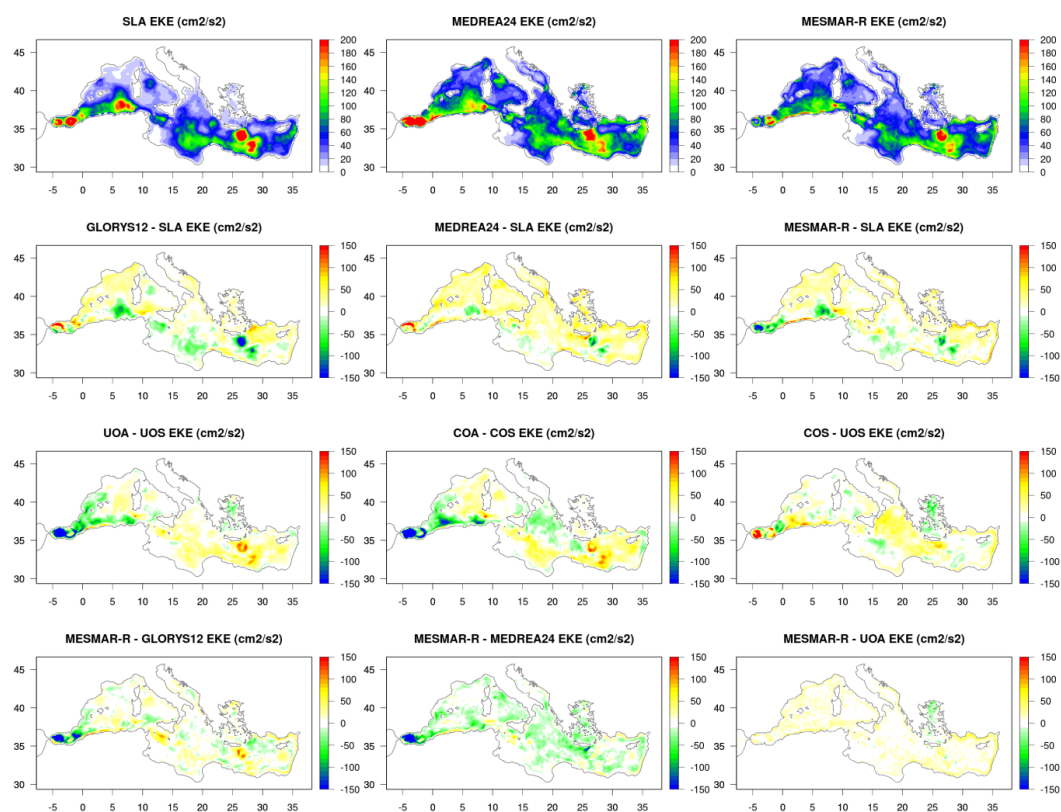
340 The sensitivity experiments highlight the contributions of individual modelling components. COA and COS exhibit higher  
341 EKE than the uncoupled systems, underscoring the tendency of coupling alone to energize the mesoscale, although, without



342 the constraint of ocean DA (COS), this may lead to less realistic variability. Conversely, UOA and UOS retain lower EKE  
343 levels, with UOS showing the weakest mesoscale activity overall, reflecting the damping imposed by prescribed atmospheric  
344 forcing and the absence of DA-induced eddy enhancement. The time series confirms this hierarchy: MESMAR-R  $\approx$  COA >  
345 COS > UOA > UOS, mirroring the combined influence of coupling and data assimilation.

346 Together, these results highlight that MESMAR-R achieves a dynamically active mesoscale field that remains close to  
347 altimetric estimates, while coupling and data assimilation jointly act to enhance EKE relative to uncoupled or unassimilated  
348 configurations.

349



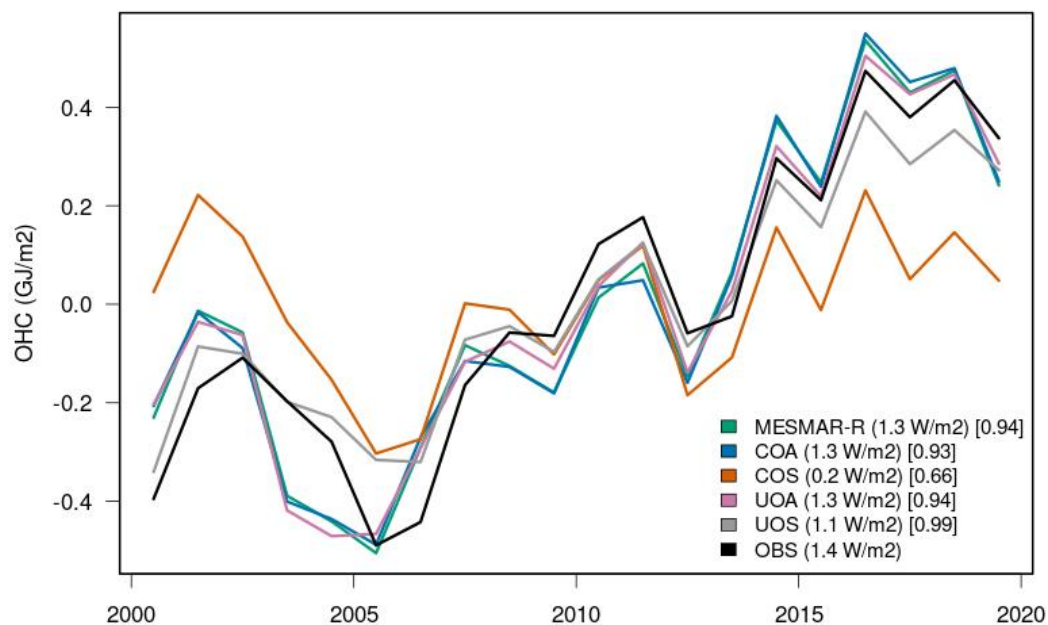
350

351 **Figure 7.** Eddy kinetic energy (EKE) maps, calculated from the MESMAR-R reanalysis, gridded altimetry data, the  
352 MEDREA24 and GLORYS12, and the sensitivity experiments, over the period 2000–2020. For all datasets, EKE is  
353 calculated from sea level, adopting the usual geostrophic relationship to calculate geostrophic currents. The top panels  
354 show the absolute EKE values, while the panels below show differences of EKE between pairs of experiments as  
355 indicated in each panel title.

356



### Yearly Ocean Heat Content Anomaly 0-700m

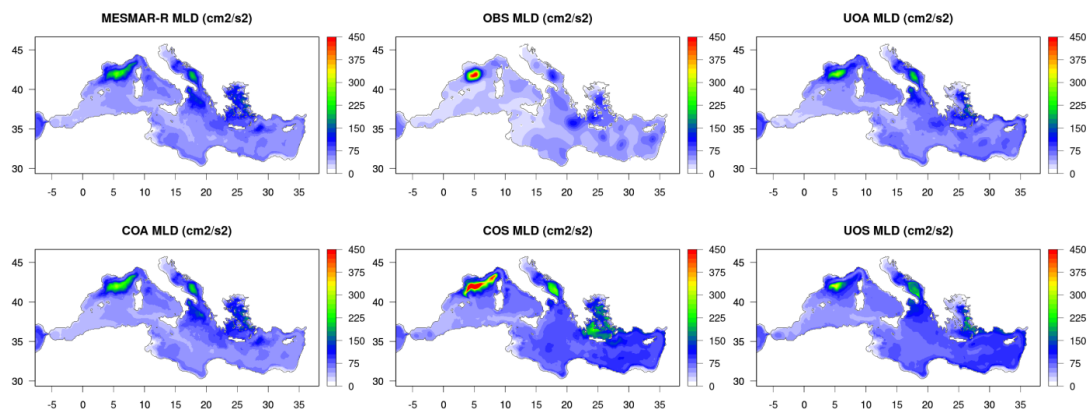


357

358 **Figure 8.** Yearly ocean heat content anomalies for the period 2000-2020 from MESMAR-R, the sensitivity experiments,  
359 and observation-based values. The legend also reports the trend in  $W\ m^{-2}$ , and the correlation with the observation-  
360 based time series.

361

362



363



364 **Figure 9. Long-term mean winter mixed layer depth (JFM) over 2000-2020 for the MESMAR-R reanalysis and the**  
365 **sensitivity experiments, together with values derived from in-situ observations.**

366

367 The evolution of ocean heat content (OHC, Figure 8 as yearly anomalies) in the upper 700 m is reproduced remarkably well  
368 by all configurations except COS, with very high correlations (0.93–0.99) relative to observed OHC estimates. The MESMAR-  
369 R, COA, and UOA simulations each display a correlation of 0.93–0.94, closely matching the amplitude and timing of observed  
370 decadal variability, while UOS performs similarly well (0.99), albeit with slightly damped interannual variability and a smaller  
371 trend. In contrast, COS shows a markedly weaker correlation (0.66), reflecting the impact of the unconstrained coupled  
372 atmosphere–ocean system, which introduces spurious variability and phase errors. The fact that MESMAR-R, COA, and UOA  
373 all produce nearly identical heat-content trends highlights that ocean data assimilation exerts the primary control on the basin-  
374 scale OHC signal, whereas coupling without DA (COS) deviates substantially. The long-term warming rate inferred from  
375 MESMAR-R, COA, and UOA ( $\sim 1.3 \text{ W m}^{-2}$ ) also closely matches the observational estimate ( $\sim 1.4 \text{ W m}^{-2}$ ), suggesting that the  
376 system’s heat uptake is robustly constrained by the assimilation of temperature and sea-level observations.

377 The mixed layer depth (MLD) fields, shown for winter (JFM), reveal a clearer impact of coupling on vertical structure (Figure  
378 9). The comparison between COS and UOS highlights that coupling deepens the mixed layer in large areas of the western  
379 Mediterranean and Levantine Basin, consistent with the enhanced wind stress and modified heat-flux patterns seen earlier.  
380 However, the addition of ocean data assimilation in COA considerably reduces these anomalies, bringing the MLD patterns  
381 closer to those of the uncoupled configurations. Similarly, MESMAR-R exhibits a more moderate MLD distribution, showing  
382 that data assimilation effectively damps the excessive deepening (or shoaling) introduced by the free coupled dynamics. This  
383 behavior mirrors the EKE results, in which coupling tends to energize the system while data assimilation restores balance:  
384 together, these findings indicate that coupling intensifies upper-ocean overturning and stratification adjustments, but  
385 assimilation acts as a strong physical constraint that controls spurious variability.

386 Taken together, the OHC and MLD diagnostics show that ocean DA provides the dominant control on basin-scale heat-content  
387 evolution, ensuring close agreement with observations, while coupling primarily modifies vertical mixing and mixed-layer  
388 dynamics, with effects that become exaggerated in the absence of data constraints. The combined MESMAR-R system  
389 therefore achieves a balanced compromise: it preserves the physically consistent surface-flux feedback of a coupled model  
390 while maintaining a realistic representation of heat storage and vertical structure through assimilation.

391 The last comparison involves ocean data assimilation increments, which are in turn a measure of systematic model errors when  
392 averaged over time (e.g., Bhargava et al., 2018). The comparison of analysis increments among the three ocean–DA-enabled  
393 configurations (MESMAR-R, COA, and UOA) provides direct insight into how strongly the data assimilation system must  
394 correct the model state in each experiment. The comparison is summarized in Figures 10 (time-averaged increments) and 11  
395 (Hovmöller diagram of spatial standard deviation over the Mediterranean Sea). Because increments represent the adjustments  
396 required to reconcile the model with observations, their time-averaged values reveal systematic model biases, whereas their  
397 spatial standard deviation quantifies how strongly and how frequently the assimilation acts. By comparing the increments  
398 across experiments, we can diagnose how coupling and atmospheric forcing influence the ocean state: if increments are smaller,  
399 the model is closer to observations, meaning that the combination of physics, coupling, and forcing used in that configuration  
400 is more self-consistent.

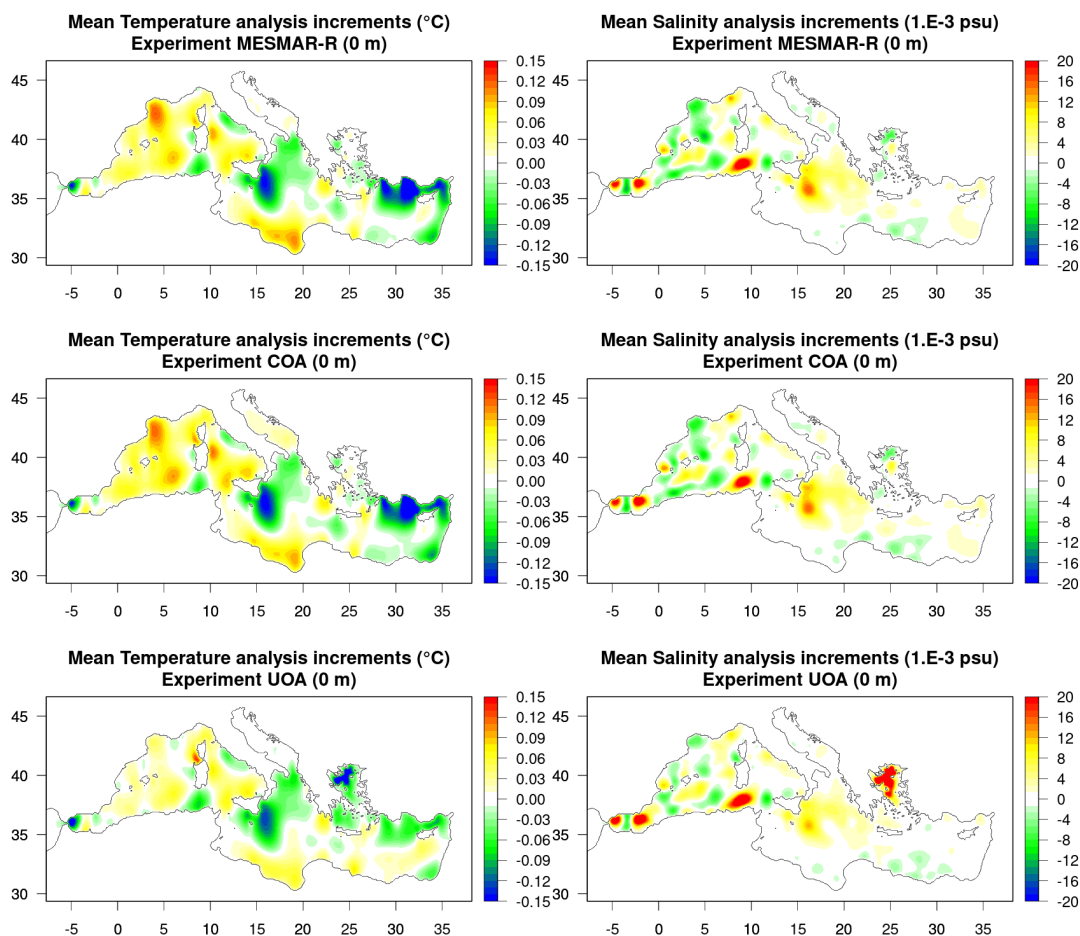


401 The time-averaged increments at the surface highlight a robust pattern present in all experiments: positive temperature  
402 increments in the western Mediterranean and negative increments in the eastern basin. This structure indicates a cold bias in  
403 the west and a warm bias in the east before analysis, consistent with the SST RMSE patterns discussed earlier. Notably, UOA  
404 shows smaller surface temperature increments than MESMAR-R or COA, especially in the central and eastern Mediterranean,  
405 confirming that the prescribed ERA5 atmospheric forcing provides a more accurate near-surface heat flux constraint than the  
406 interactive coupling. UOA increments are, however, consistent in sign with those from MESMAR-R, showcasing persistent  
407 biases likely originating in the ocean model component. This result aligns with the surface flux analysis, where coupling  
408 produced regional discrepancies in latent and sensible heat fluxes, particularly in the Levantine and Aegean Seas.

409 For salinity at 0 m, the increments again show broad similarities across experiments, but UOA displays a distinct freshening  
410 increment in the Aegean Sea that is not present in the coupled configurations. This feature likely reflects the fresh bias  
411 introduced by ERA5 freshwater forcing, which lacks the dynamically consistent evaporation–precipitation adjustments of the  
412 coupled system. It also echoes earlier findings that coupling improves SSS in the Aegean by enhancing realistic evaporative  
413 fluxes and, to a lesser extent, river discharge. These consistencies strengthen the interpretation that salinity is especially  
414 sensitive to air–sea freshwater coupling, whereas temperature is more sensitive to heat-flux accuracy.

415 At 30 m and 100 m (not shown), the differences among experiments are substantially reduced. The increments remain spatially  
416 coherent but become weaker and less distinct across configurations, indicating that the influence of atmospheric forcing and  
417 coupling diminishes rapidly below the surface mixed layer. Nevertheless, a persistent feature across all three experiments is  
418 the salinity correction in the southwestern Mediterranean, which likely reflects biases in the water exchanged through the Strait  
419 of Gibraltar, consistently with the EKE and SSS anomalies noted near the entrance of the basin. Beyond this, the experiments  
420 converge, confirming that the main differences between configurations are confined to the upper ~50 m, where coupling and  
421 surface fluxes exert the strongest control.

422



423

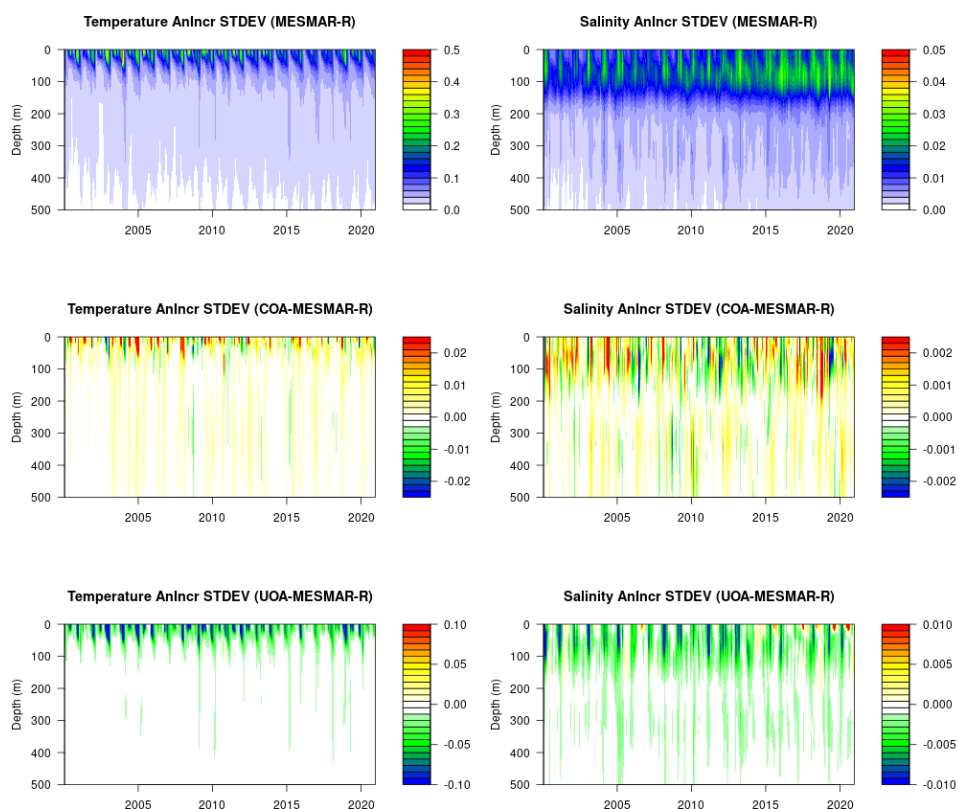
424 **Figure 10. Time-averaged analysis increments at the sea surface for MESMAR-R and the other two experiments with**  
425 **ocean data assimilation enabled. The period is 2000-2020.**

426

427 The Hovmöller diagrams (Figure 11) further clarify the behavior of the assimilation system. In MESMAR-R, temperature  
428 increments peak in summer, when strong stratification makes the model more sensitive to surface forcing errors and limits  
429 vertical redistribution of heat. Over time, a modest decrease in increment magnitude is evident, suggesting that the reanalysis  
430 improves internally throughout the period, likely via better-constrained large-scale circulation and gradual spin-up of the  
431 coupled and data assimilation systems.

432 For salinity, MESMAR-R exhibits larger increment variability, particularly in the upper 100 m. Part of this arises from the  
433 greater density of salinity observations (ARGO, gliders, ship-based), but it also reflects the intrinsic sensitivity of  
434 Mediterranean salinity to evaporation, runoff, and mixing, all of which contribute to persistent local biases.

435



436

437 **Figure 11. Hovmöller diagram (time-depth) of the analysis increment spatial standard deviation for MESMAR-R and**  
438 **the other two experiments with ocean data assimilation enabled. The period is 2000-2020.**

439

440 Differences relative to MESMAR-R provide further insight. The COA minus MESMAR-R differences are slightly positive  
441 almost everywhere, confirming that the atmospheric DA included in MESMAR-R marginally reduces the need for ocean  
442 corrections. This reinforces earlier conclusions that atmospheric assimilation improves the air–sea flux balance, particularly  
443 for heat and freshwater, thereby generally reducing ocean misfits.

444 Conversely, UOA minus MESMAR-R differences show generally negative values in the upper 50 m, consistent with the higher  
445 fidelity of ERA5 forcing for near-surface fields. These differences peak in winter, when atmospheric forcing dominates mixed-  
446 layer dynamics, and coupling errors can accumulate most easily. Below ~50 m, the differences vanish, reinforcing that ERA5  
447 and coupling primarily diverge near the surface.

448

449

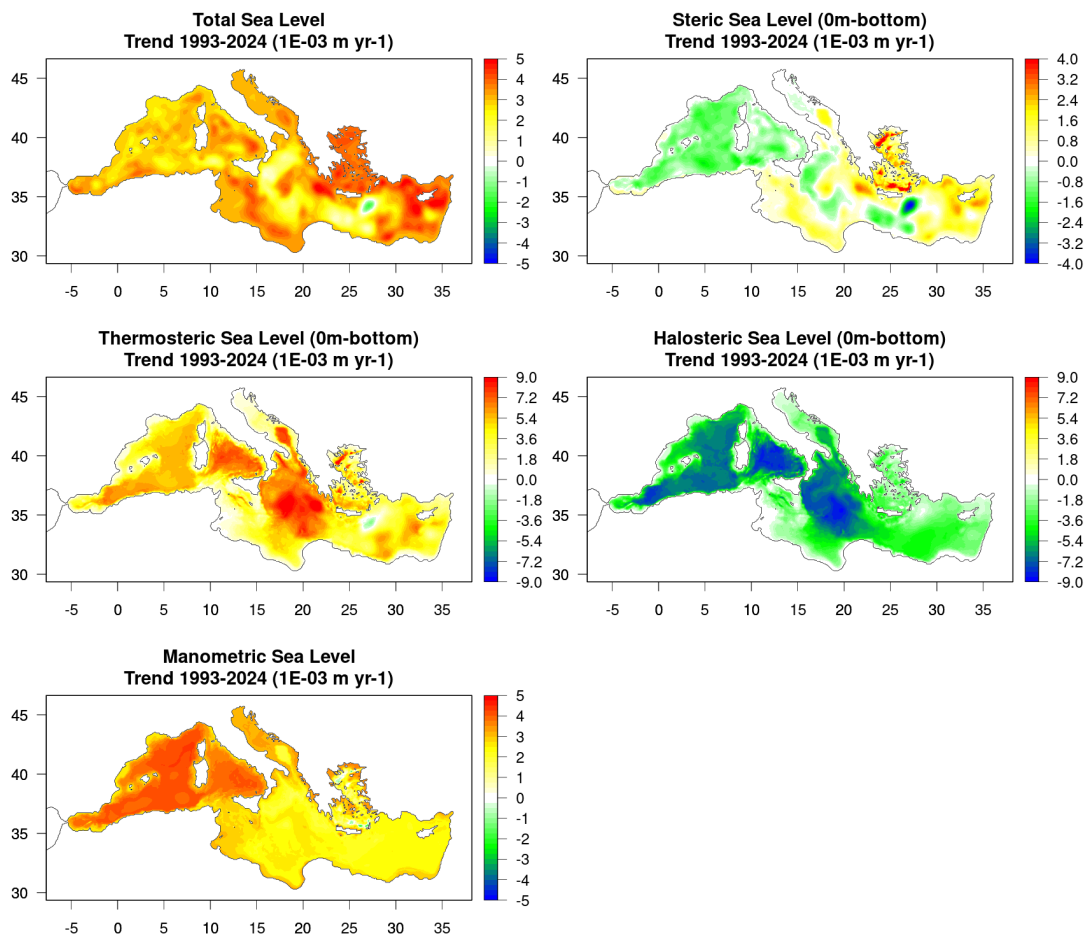


450 **5. Climate indices**

451 **5.1 Oceanic long-term changes from the MESMAR-R Reanalysis**

452 The MESMAR-R coupled reanalysis provides a dynamically consistent multidecadal reconstruction of the Mediterranean  
453 circulation and its climate evolution over 1993–2024. Beyond the validation metrics discussed previously, the long-term trends  
454 in sea level, temperature, salinity, and heat/salt content offer a representation of the climate response of the Mediterranean  
455 basin. The Mediterranean is a semi-enclosed concentration basin whose thermohaline characteristics evolve rapidly under  
456 climate forcing, and where salinity-driven density changes can dominate over thermal effects. The climate indices derived  
457 from MESMAR-R are therefore particularly informative in assessing regional climate changes.

458



459

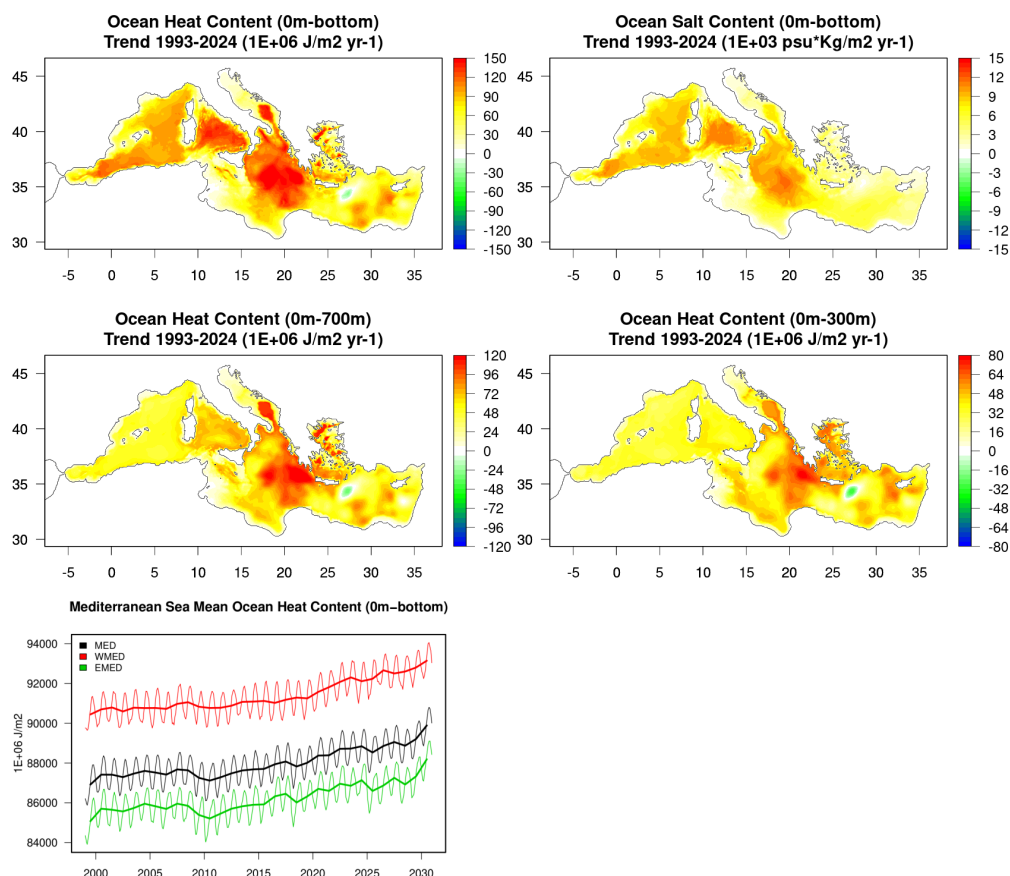
460 **Figure 12. Maps of linear trends (1993-2024) for sea level and its components, from MESMAR-R.**

461



462 The halosteric component of sea level exhibits a strong, basin-wide negative trend in MESMAR-R, with a basin-mean decrease  
463 of approximately  $-3.87 \text{ mm yr}^{-1}$  over 1993–2024 and even stronger halosteric decline in the western basin ( $-5.02 \text{ mm yr}^{-1}$ )  
464 relative to the eastern basin ( $-3.27 \text{ mm yr}^{-1}$ ) (see Figure 12 and Table 4). These values are fully consistent with the intensifying  
465 salinification of the Mediterranean reported in observational and modelling studies (Liu et al., 2025; Skliris et al., 2018;  
466 Aydogdu et al., 2023). The trend maps show particularly strong halosteric lowering in the Alboran Sea and western  
467 Mediterranean gyre, a region identified in previous work as a hotspot of salinity-driven density increase, likely associated with  
468 enhanced evaporation and changes in Atlantic inflow properties (Skliris et al., 2018). A pronounced east–west contrast persists  
469 across depth, indicating that salinity anomalies penetrate well into intermediate waters, consistent with evidence of progressive  
470 warming and salinification of Levantine Intermediate Water (Pinardi and Masetti, 2000; Margirier et al., 2020). This halosteric  
471 signal strongly compensates for the thermosteric rise, leading to the well-known thermo–halo compensation characteristic of  
472 the Mediterranean (Liu et al., 2025). Local features such as weaker halosteric trends in the Adriatic, influenced by river  
473 discharge and dense-water formation, further corroborate the realism of MESMAR-R.

474

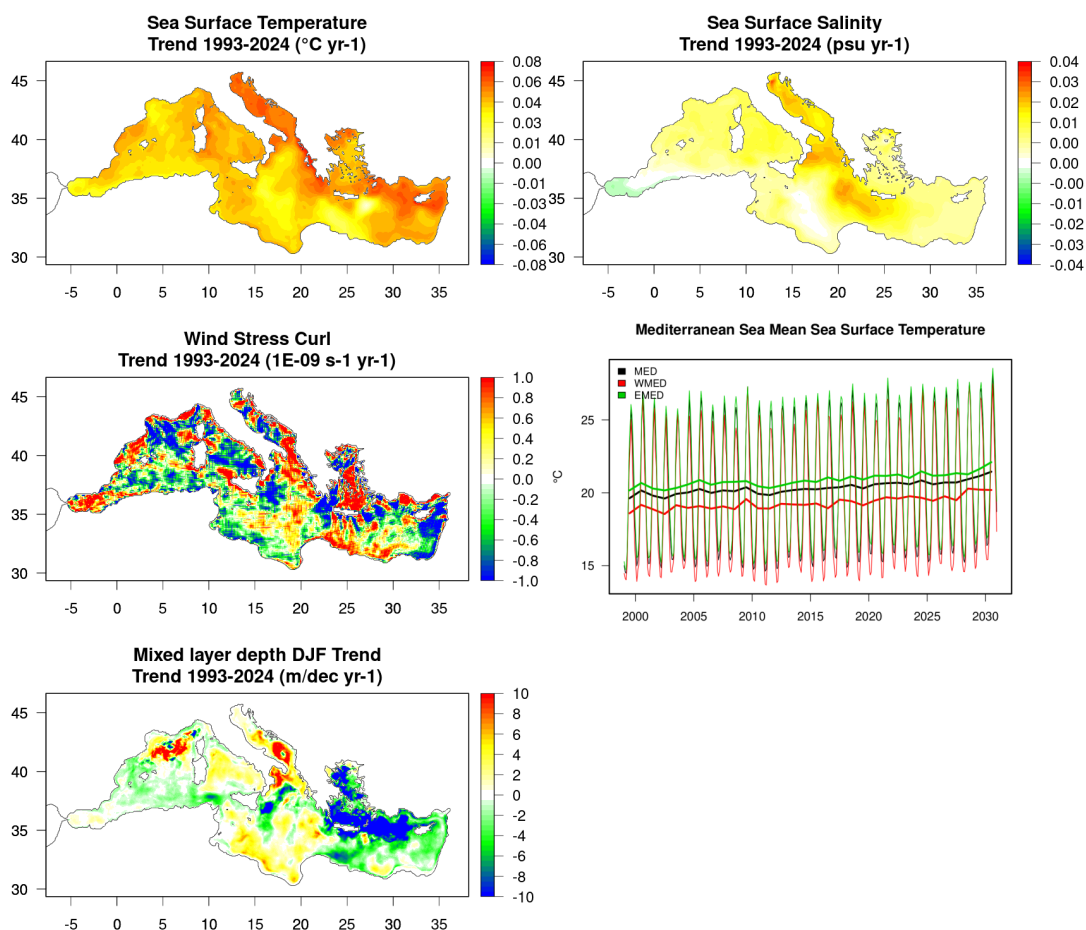


475

476 **Figure 13. Maps of linear trends (1993-2024) for ocean heat and salt content, and OHC timeseries from MESMAR-R**



477 The decomposition of sea-level rise into steric and manometric components (by difference) shows that basin-mean  
 478 Mediterranean sea-level rise in MESMAR-R is dominated by mass changes rather than steric contributions, i.e., the basin's  
 479 response to the Atlantic sea-level rise via exchanges through the Strait of Gibraltar. The basin-average total sea-level trend of  
 480 approximately  $3.06 \text{ mm yr}^{-1}$  is in excellent agreement with the Copernicus Marine Service Mediterranean Sea Level Indicator  
 481 and with external literature estimates ranging from 2.5 to  $4.0 \text{ mm yr}^{-1}$  (Calafat et al., 2012; Marcos & Tsimplis, 2008). By  
 482 contrast, the manometric sea level rise is equal to  $2.88 \text{ mm yr}^{-1}$ , accounting for 94% of the sea level rise over 1993-2024 and  
 483 in agreement with independent estimates based on independent sea level budget analysis (Storto et al., 2024). Wind-stress-curl  
 484 trends in MESMAR-R do not appear to exert a first-order control on the basin-mean sea-level rise; however, positive curl  
 485 anomalies over parts of the eastern Mediterranean (Figure 14) may contribute locally to the intermediate-layer warming signal.  
 486



487

488 **Figure 14. Maps of linear trends (1993-2024) for selected variables, and time series of SST, from MESMAR-R.**

489 The basin-average ocean heat content (OHC in the top 700m, Figure 13 and Table 1) trend from MESMAR-R is  $1.10 (1.34)$   
 490  $\text{W m}^{-2}$  for the period 1993-2024 (1999-2024), in line with recent observational and reanalysis-based assessments (Pisano et  
 491 al., 2020; von Schuckmann et al., 2016). MESMAR-R also captures the characteristic east–west contrast in heat-content  
 24



492 evolution, with stronger warming and larger fluctuations in the eastern basin, particularly in the Levantine and Ionian regions.  
 493 Trend maps show spatially coherent warming extending from the surface to intermediate depths (~300–700 m), associated  
 494 with the warming and deep penetration of LIW. The implied vertical structure is consistent with the findings of Margirier et  
 495 al. (2020), who documented an abrupt warming and salinification of intermediate waters beginning in the early 2000s. The  
 496 warming pattern in MESMAR-R aligns with the basin’s sensitivity to changes in surface heat fluxes and stratification, and the  
 497 weak wind-stress-curl trends suggest that mechanical forcing plays a secondary role compared with thermohaline adjustments.  
 498

Variable	Basin-mean trend	Western Mediterranean	Eastern Mediterranean
Total Sea Level (mm yr <sup>-1</sup> )	3.61 (3.06)	3.73 (2.94)	3.54 (3.13)
Thermosteric SL (mm yr <sup>-1</sup> )	5.04 (4.03)	5.29 (4.29)	4.91 (3.89)
Halosteric SL (mm yr <sup>-1</sup> )	-4.21 (-3.87)	-5.23 (-5.02)	-3.68 (-3.27)
Steric (total) (mm yr <sup>-1</sup> )	0.82 (0.18)	0.11 (-0.67)	1.19 (0.62)
Manometric SL (mm yr <sup>-1</sup> )	2.79 (2.88)	3.62 (3.61)	2.35 (2.51)
OHC (0–700 m) (W m <sup>-2</sup> )	1.34 (1.10)	1.28 (0.94)	1.37 (1.18)
OHC (0–bottom) (W m <sup>-2</sup> )	2.05 (1.68)	2.05 (1.55)	2.04 (1.75)
SSS trend (psu yr <sup>-1</sup> )	0.008 (0.011)	0.007 (0.009)	0.009 (0.012)
SST trend (°C yr <sup>-1</sup> )	0.055 (0.048)	0.056 (0.047)	0.055 (0.049)
Salt Content (psu·kg m <sup>-2</sup> yr <sup>-1</sup> )	5.68×10 <sup>3</sup> (5.22 ×10 <sup>3</sup> )	7.02×10 <sup>3</sup> (6.75 ×10 <sup>3</sup> )	4.98×10 <sup>3</sup> (4.42 ×10 <sup>3</sup> )

499 **Table 4. Mediterranean Sea-averaged long-term trends over the periods 1999–2024 (1993–2024 in parentheses),**  
 500 **separated for the entire basin, the western and eastern basins as defined in section 2.4.**

501

502 **5.2 Atmospheric long-term changes from the MESMAR-R Reanalysis**

503 The trends in near-surface atmospheric variables over 1993–2024 (Figure 15 and Table 5) depict a Mediterranean–southern  
 504 Europe climate signal that is fully consistent with the “hot-spot” character of the region described in previous work (Giorgi &  
 505 Lionello, 2008; MedECC, 2020). In winter (DJF), 2-m air temperature shows a robust warming over almost the entire domain,  
 506 with maxima over central and eastern Europe and weaker positive trends over the Mediterranean Sea itself; this corresponds  
 507 well to the MED-average DJF warming of +0.040 °C yr<sup>-1</sup>. Precipitation trends are more heterogeneous, with modest drying  
 508 over much of the western and central Mediterranean and parts of North Africa, and localized increases along the northern  
 509 mountain ranges (e.g., Alps-Dinaric arc), in line with earlier observational and modelling studies that report winter  
 510 precipitation decreases over the Mediterranean land areas but more mixed signals at higher latitudes and elevations (Hoerling  
 511 et al., 2012; Hertig, 2017; Beranová et al., 2025). Column-integrated precipitable water increases almost everywhere in DJF  
 512 (+0.023 % yr<sup>-1</sup> increase on average), while near-surface relative humidity shows a dipole structure, with slight moistening over



513 northern Europe and drying over the southern flanks of the basin. These changes point to a more moisture-laden but thermally  
 514 driven winter atmosphere in which enhanced water vapour does not systematically translate into increased mean precipitation  
 515 (with an average DJF precipitation trend of  $+2.2 \times 10^{-3} \text{ mm day}^{-1} \text{ yr}^{-1}$ ), consistent with recent moisture-budget analyses based  
 516 on ERA5 that highlight the dominant role of transient processes in transporting oceanic moisture onto surrounding land  
 517 (Tootoonchi et al., 2025).

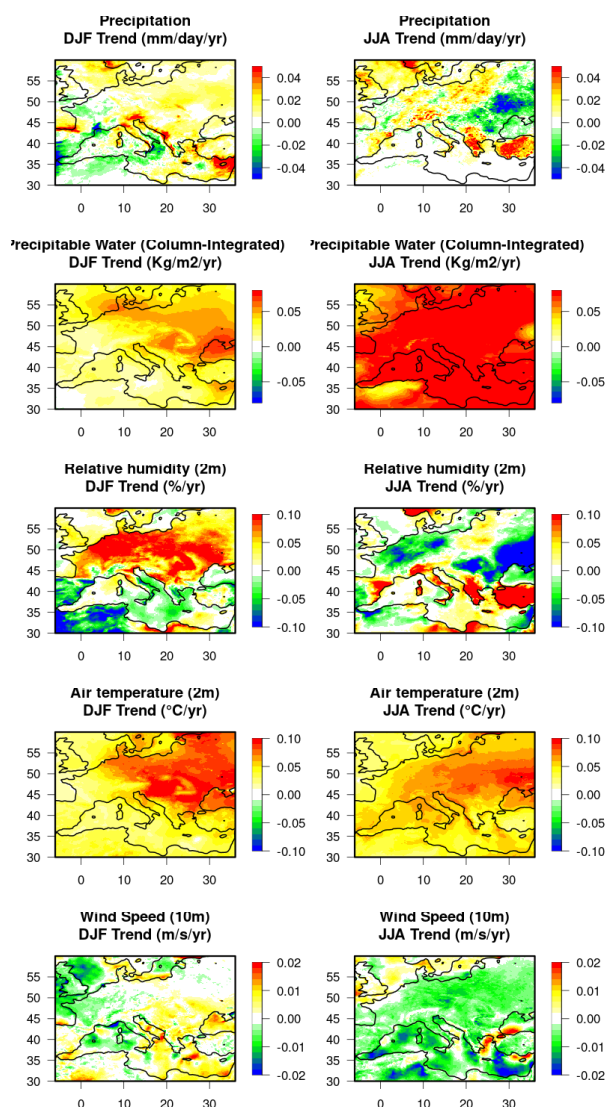


**Figure 15. Winter (DJF) and summer (JJA) trends of selected atmospheric variables from MESMAR-R, computed over the period 1993-2024.**

518

519 Summer (JJA) trends display an even clearer expression of Mediterranean aridification. Near-surface temperature increases  
 520 are larger than in winter in southern Europe and the Mediterranean region, and exhibit a strong meridional gradient (average  
 521 JJA warming of  $+0.047 \text{ °C yr}^{-1}$ , in line with projections and recent assessments of compound hot–dry summers over the region,  
 522 i.e., Giorgi & Lionello, 2008; Lhotka et al., 2023; MedECC, 2020). Mean precipitation shows heterogeneous behavior, with



523 neutral tendency in the southern Mediterranean and mixed above; at the same time, precipitable water exhibits strong positive  
 524 trends over essentially the whole domain (average JJA trend of  $+0.100 \text{ \% yr}^{-1}$ ) while near-surface relative humidity decreases  
 525 over large parts of Europe while the southern Mediterranean shows a small increase. This combination of higher column water  
 526 vapour, lower relative humidity, and reduced mean precipitation is typical of a warming, drying regime where the atmosphere  
 527 can hold more moisture (Hoerling et al., 2012; González-Hidalgo et al., 2025; Figueiredo et al., 2025) but does not necessarily  
 528 precipitate more often, instead favouring longer dry spells punctuated by intense events (Zittis et al., 2021; Senatore et al.,  
 529 2025).

530

Variable	DJF	MAM	JJA	SON
<b>10m Wind Speed</b> ( $\text{cm s}^{-1} \text{ yr}^{-1}$ )	0.20	0.30	-0.45	-0.37
<b>2m Temperature</b> ( $^{\circ}\text{C yr}^{-1}$ )	0.040	0.037	0.047	0.053
<b>2m Relative Humidity</b> ( $\% \text{ yr}^{-1}$ )	-0.017	0.008	0.027	-0.006
<b>Precipitable Water</b> ( $\% \text{ yr}^{-1}$ )	0.023	0.043	0.100	0.070
<b>Total Precipitation</b> (mm $\text{day}^{-1} \text{ yr}^{-1}$ )	2.2 E-3	4.3 E-3	4.2 E-3	-0.36 E-3

531 **Table 5. Mediterranean region-averaged trends for the four seasons and selected variables, from MESMAR-R over the**  
 532 **period 1993-2024. The region is defined as 30–45°N, 10°W–40°E (land and sea combined), close to the domain used by**  
 533 **Giorgi and Lionello (2008) but without the Alpine region.**

534 The trends in 10-m wind speed are comparatively modest, but they exhibit coherent regional structures that can lead to changes  
 535 in winter oceanic mixed-layer depth (MLD, Figure 14). In DJF, MESMAR-R shows localized increases in surface wind speed  
 536 over the Gulf of Lion and parts of the northern Ionian/Aegean, consistent with the average DJF trend of  $+0.20 \text{ cm s}^{-1} \text{ yr}^{-1}$   
 537 together with small negative temperature trends relative to surrounding regions. These areas coincide with positive DJF MLD  
 538 trends, indicating a deepening of the winter mixed layer that is consistent with enhanced mechanical mixing and stronger  
 539 buoyancy loss. Conversely, in the Levantine and southeastern Mediterranean, winter MLD trends are negative (shoaling) and  
 540 co-occur with marked warming and slight wind weakening, suggesting reduced buoyancy loss and a decline in deep or  
 541 intermediate-water formation. The large-scale wind-stress-curl trends derived earlier show only modest changes, but positive  
 542 curl anomalies in parts of the eastern basin support a dynamical picture in which circulation adjustments and stratification  
 543 changes modulate the mixed-layer response on top of local surface-flux trends.

544



## 545 5. Discussion and Conclusions

546 Achieving a dynamically consistent reconstruction of the recent atmosphere-ocean-hydrology evolution over the  
547 Mediterranean region, one of the world's most prominent climate-change hotspots, is essential for disentangling the processes  
548 that govern its regional response to global warming. Here, we have presented one of the first regional coupled reanalyses  
549 produced to date, to our knowledge. The regional reanalysis system, called MESMAR-R, features state-of-the-art ocean,  
550 weather, and river discharge numerical models, complemented with data assimilation systems in both the atmosphere and the  
551 ocean, although these are weakly coupled in the sense that observations in one medium do not directly affect analysis  
552 corrections in the other medium. The atmospheric data assimilation is somewhat simple (based on three-dimensional nudging);  
553 yet the system provides an atmosphere-ocean-consistent reconstruction of the latest 32 years (1993-2024).

554 The ocean component of MESMAR-R embeds an advanced variational data assimilation system and demonstrates clear  
555 strengths at the surface and in the upper ocean, particularly for sea level, sea surface salinity, and upper-layer temperature.  
556 These results confirm the quality of the new reanalysis in the layers most relevant to air-sea interaction and marine variability.  
557 Remaining differences in mid-depth temperature suggest areas for further improvement, possibly linked to intermediate-water  
558 representation. The spatial patterns of skill scores reinforce the basin-wide good performances of MESMAR-R at the sea  
559 surface, with the clearest benefits relative to external products, especially for salinity and sea level. Localized degradations  
560 (e.g., in the northern Adriatic and Aegean Seas) suggest areas where representation of strong riverine inputs and complex  
561 circulation could be further optimized.

562 Overall, the atmospheric evaluation confirms that MESMAR-R performs reasonably well given its simplified atmospheric data  
563 assimilation approach. While its near-surface atmospheric variables generally exhibit higher RMSE than those from ERA5  
564 and CERRA, the differences remain moderate, and the fields are of comparable quality at the basin's scale. Localized  
565 improvements indicate that the coupled system can maintain internally consistent air-sea interactions despite the limited  
566 atmospheric assimilation. These results demonstrate that, although MESMAR-R does not aim to compete with dedicated  
567 atmospheric reanalyses, its atmospheric component provides a physically coherent and sufficiently accurate representation of  
568 the Mediterranean climate to support further process-oriented investigations.

569 Several sensitivity tests were conducted to disentangle the impact of coupling and data assimilation in MESMAR-R. These  
570 demonstrate that data assimilation in both components is essential for optimal coupled performance. MESMAR-R achieves  
571 the best compromise between realism and stability, with coupling improving certain surface metrics (notably salinity) and  
572 atmospheric data assimilation further enhancing the representation of SST and SLA. The results collectively highlight that  
573 while coupling alone is not sufficient to match the reanalysis skill, it becomes most effective when supported by data  
574 assimilation in both the ocean and atmosphere. The sensitivity experiments indicate that coupling most strongly affects regions  
575 where the air-sea humidity and wind-speed fields are highly sensitive to ocean-atmosphere feedback, with evaporation acting  
576 as the primary mediator of salinity changes. The results are consistent with the RMSE analysis, where coupling intensifies  
577 latent heat losses (e.g., Aegean and parts of the eastern Mediterranean), and coupled configurations outperform uncoupled  
578 ones. This was also strengthened by the assessment of the analysis increments whose averaged signal primarily responds to  
579 systematic error corrections.

580 The analysis of oceanic trends demonstrates that MESMAR-R has provided a coherent and physically consistent reconstruction  
581 of Mediterranean climate evolution over the past three decades. The reanalysis captures the basin-wide salinification, the  
582 thermo-halo compensation of steric sea-level change, the mass-driven nature of Mediterranean sea-level rise, and a heat-  
583 content increase fully aligned with observational estimates. Long-term atmospheric trends from MESMAR-R (1993-2024)



584 reveal a climate signal fully consistent with the well-documented Mediterranean hot-spot behavior. Winter and summer both  
585 exhibit pronounced near-surface warming, widespread drying, and strong moistening of the atmospheric column, confirming  
586 the thermodynamic intensification of the regional hydrological cycle.

587 MESMAR-R, while presenting room for further improvement in the future (more advanced atmospheric data assimilation and  
588 air-sea balanced corrections), represents a unique reconstruction of the past climate in the Mediterranean region with more  
589 dynamically consistent atmospheric and oceanic fields than in uncoupled systems. Its ocean-focused design mirrors state-of-  
590 the-art performance for the ocean component, despite its moderate spatial resolution. The primary advantage of the MESMAR-  
591 R reanalysis is, however, the balanced response across the atmosphere and the ocean in the Mediterranean Sea, which makes  
592 it a valuable product to assess compound events in the region, and any other strongly coupled air-sea process, including, e.g.,  
593 medicanes and heavy precipitation events.

594



595 **Data availability:** The MESMAR-R reanalysis data files used in this study are available for download from Storto et al. (2025)  
596 [<https://doi.org/10.5281/zenodo.17829847>]. Such data records contain monthly mean fields, and data assimilation files  
597 (observation innovation and statistics, analysis increments), together with post-processed data as used in the manuscripts  
598 (linear trends). Higher-frequency fields (6-hourly), not used in this study but produced, are available on request from the  
599 authors and are planned to be published in institutional data hubs soon.

600 **Code availability:** The NEMO ocean model code (v4.0.7) is available at <https://forge.ipsl.jussieu.fr/nemo/wiki> (NEMO,  
601 2023), the WRF atmospheric model code (v4.3.3) is available at <https://github.com/wrf-model/WRF> (wrf-model, 2023), and  
602 the HD hydrological discharge model (v5.1) is available at <https://doi.org/10.5281/zenodo.5707587> (Hagemann and Ho-  
603 Hagemann, 2021). The frozen version of the MESMAR v1 code used in this paper is available at  
604 <https://doi.org/10.5281/zenodo.7898938> (Storto et al., 2023). The ocean variational data assimilation is available at:  
605 [https://baltig.cnr.it/nemo\\_ismar-rm/3dvar](https://baltig.cnr.it/nemo_ismar-rm/3dvar). Specific configuration files of the models and coupler used within this study are  
606 contained in the dataset record (Storto et al., 2025).

607 **Author contribution:** AS and VdT developed the regional coupled model; AS and CY designed the study; AS performed the  
608 reanalysis and the sensitivity experiments; AS prepared the manuscript with contributions from all co-authors.

609 **Competing interests:** At least one of the (co-)authors serves as editor for the special issue to which this paper belongs.

#### 610 **Acknowledgements**

#### 611 **Financial support**

612 This research is supported by programme CN00000013, the “National Centre for HPC, Big Data and Quantum Computing”  
613 Directorial Decree (grant no. 1031 of 17 June 2022), from the resources of the PNRR MUR – M4C2 – Investment 1.4 –  
614 “National Centers” Directorial Decree (grant no. 3138 of 16 December 2021).

615



616 **References**

- 617 Adler, R.F., Huffman, G.J., Chang, A., Ferraro, R., Xie, P., Janowiak, J., Rudolf, B., Schneider, U., Curtis, S., Bolvin, D.,  
618 Gruber, A., Susskind, J., and Arkin, P.: The Version-2 Global Precipitation Climatology Project (GPCP) Monthly Precipitation  
619 Analysis (1979–Present). *J. Hydrometeor.*, 4, 1147–1167, [https://doi.org/10.1175/1525-7541\(2003\)004<1147:TVGPCP>2.0.CO;2](https://doi.org/10.1175/1525-7541(2003)004<1147:TVGPCP>2.0.CO;2), 2003.
- 621 Akhtar, N., Brauch, J., Dobler, A., Béranger, K., and Ahrens, B.: Medicanes in an ocean–atmosphere coupled regional climate  
622 model, *Nat. Hazards Earth Syst. Sci.*, 14, 2189–2201, <https://doi.org/10.5194/nhess-14-2189-2014>, 2014.
- 623 Aydogdu, A., Miraglio, P., Escudier, R., Clementi, E., and Masina, S.: The dynamical role of upper layer salinity in the  
624 Mediterranean Sea, in: 7th edition of the Copernicus Ocean State Report (OSR7), von Schuckmann, K. et al. (Eds.), Copernicus  
625 Publications, State Planet, 1-osr7, 6, <https://doi.org/10.5194/sp-1-osr7-6-2023>, 2023.
- 626 Ballarotta, M., Ubelmann, C., Veillard, P., Prandi, P., Etienne, H., Mulet, S., Faugère, Y., Dibarboue, G., Morrow, R., and  
627 Picot, N.: Improved global sea surface height and current maps from remote sensing and in situ observations, *Earth Syst. Sci.*  
628 *Data*, 15, 295–315, <https://doi.org/10.5194/essd-15-295-2023>, 2023.
- 629 Beranová, R., Huth, R., and Vít, V.: A multidataset analysis of precipitation trends in Europe, *J. Hydrometeorol.*, 26, 1003–  
630 1015, <https://doi.org/10.1175/JHM-D-24-0114.1>, 2025.
- 631 Bhargava, K., Kalnay, E., Carton, J. A., and Yang, F.: Estimation of systematic errors in the GFS using analysis increments.  
632 *J. Geophys. Res.-Atmos.*, 123, 1626–1637, <https://doi.org/10.1002/2017JD027423>, 2018.
- 633 Brewin, R. J. W., Sathyendranath, S., Jackson, T., Barlow, R., Brotas, V., Airs, R., and Lamont, T.: Influence of light in the  
634 mixed-layer on the parameters of a three-component model of phytoplankton size class, *Remote Sens. Environ.*, 168, 437–  
635 450, <https://doi.org/10.1016/j.rse.2015.07.004>, 2015.
- 636 Calafat, F. M., Chambers, D. P., and Tsimplis, M. N.: Mechanisms of decadal sea level variability in the eastern North Atlantic  
637 and the Mediterranean Sea, *J. Geophys. Res.-Oceans*, 117, C09022, <https://doi.org/10.1029/2012JC008285>, 2012.
- 638 Camus, P., Haigh, I. D., Nasr, A. A., Wahl, T., Darby, S. E., and Nicholls, R. J.: Regional analysis of multivariate compound  
639 coastal flooding potential around Europe and environs: sensitivity analysis and spatial patterns, *Nat. Hazards Earth Syst. Sci.*,  
640 21, 2021–2040, <https://doi.org/10.5194/nhess-21-2021-2021>, 2021.
- 641 Canuto, V. M., Howard, A., Cheng, Y., and Dubovikov, M. S.: Ocean turbulence. Part I: One-point closure model—momentum  
642 and heat vertical diffusivities, *J. Phys. Oceanogr.*, 31, 1413–1426, 2001.
- 643 Choi, Y.-S., and Lee, D.-K.: Spectral nudging to the global reanalysis data in the WRF regional model, *Asia-Pac. J. Atmos.*  
644 *Sci.*, 52, 135–150, <https://doi.org/10.1007/s13143-016-0004-9>, 2016.
- 645 Craig, A. P., Valcke, S., and Coquart, L.: Development and performance of a new version of the OASIS coupler, OASIS3-  
646 MCT\_3.0, *Geosci. Model Dev.*, 10, 3297–3308, <https://doi.org/10.5194/gmd-10-3297-2017>, 2017.
- 647 Cramer, W., Guiot, J., Fader, M., et al.: Climate change and interconnected risks to sustainable development in the  
648 Mediterranean, *Nat. Clim. Change*, 8, 972–980, <https://doi.org/10.1038/s41558-018-0299-2>, 2018.
- 649 de Figueiredo, D. R., Bento, S., and Condesso de Melo, M. T.: Freshwater quality challenges in southern Europe under an  
650 increasingly warmer and drier climate scenario, *Water*, 17, 1873, <https://doi.org/10.3390/w17131873>, 2025.



- 651 Doury, A., Somot, S., Gadat, S., et al.: Regional climate model emulator based on deep learning: concept and first evaluation  
652 of a novel hybrid downscaling approach, *Clim. Dyn.*, 60, 1751–1779, <https://doi.org/10.1007/s00382-022-06343-9>, 2023.
- 653 Escudier, R., Clementi, E., Cipollone, A., Pistoia, J., Drudi, M., Grandi, A., Lyubartsev, V., Lecci, R., Aydogdu, A., Delrosso,  
654 D., Omar, M., Masina, S., Coppini, G., and Pinaridi, N.: A high-resolution reanalysis for the Mediterranean Sea, *Front. Earth  
655 Sci.*, 9, 702285, <https://doi.org/10.3389/feart.2021.702285>, 2021.
- 656 Fox-Hughes, P., Su, C.-H., Eizenberg, N., et al.: A review of early severe weather applications of high-resolution regional  
657 reanalysis in Australia, *Meteorol. Appl.*, 29, e2087, <https://doi.org/10.1002/met.2087>, 2022.
- 658 Giorgi, F., and Lionello, P.: Climate change projections for the Mediterranean region, *Global Planet. Change*, 63, 90–104,  
659 2008.
- 660 González-Hidalgo, J. C., and Vicente-Serrano, S. M.: Is there a precipitation decline in the Mediterranean region? An  
661 assessment based on the scientific literature, *Int. J. Climatol.*, 45, e8918, <https://doi.org/10.1002/joc.8918>, 2025.
- 662 Good, S. A., Martin, M. J., and Rayner, N. A.: EN4: quality controlled ocean temperature and salinity profiles and monthly  
663 objective analyses with uncertainty estimates, *J. Geophys. Res.-Oceans*, 118, 6704–6716,  
664 <https://doi.org/10.1002/2013JC009067>, 2013.
- 665 Hagemann, S., and Dümenil Gates, L.: Validation of the hydrological cycle of ECMWF and NCEP reanalyses using the MPI  
666 hydrological discharge model, *J. Geophys. Res.-Atmos.*, 106, 17901–17917, <https://doi.org/10.1029/2000JD900568>, 2001.
- 667 Hagemann, S., Ho-Hagemann, H. T. M., and Rechid, D.: The hydrological discharge model (HD model, version 5.1) –  
668 description and technical documentation, *Zenodo*, <https://doi.org/10.5281/zenodo.5707587>, 2020.
- 669 Haylock, M. R., Hofstra, N., Klein Tank, A. M. G., Klok, E. J., Jones, P. D., and New, M.: A European daily high-resolution  
670 gridded data set of surface temperature and precipitation for 1950–2006, *J. Geophys. Res.-Atmos.*, 113, D20119, 2008.
- 671 Hersbach, H., Bell, B., Berrisford, P., et al.: The ERA5 global reanalysis, *Q. J. Roy. Meteor. Soc.*, 146, 1999–2049,  
672 <https://doi.org/10.1002/qj.3803>, 2020.
- 673 Hertig, E., and Trambly, Y.: Regional downscaling of Mediterranean droughts under past and future climatic conditions,  
674 *Global Planet. Change*, 151, 36–48, <https://doi.org/10.1016/j.gloplacha.2016.10.015>, 2017.
- 675 Hoerling, M., Eischeid, J., Perlwitz, J., Quan, X., Zhang, T., and Pegion, P.: On the increased frequency of Mediterranean  
676 drought, *J. Climate*, 25, 2146–2161, <https://doi.org/10.1175/JCLI-D-11-00296.1>, 2012.
- 677 Jousset, S., Mulet, S., Greiner, E., et al.: New global mean dynamic topography CNES-CLS-22 combining drifters,  
678 hydrography profiles and high frequency radar data, *ESS Open Archive*,  
679 <https://doi.org/10.22541/essoar.170158328.85804859/v2>, 2025.
- 680 Juza, M., Fernández-Mora, À., and Tintoré, J.: Sub-regional marine heat waves in the Mediterranean Sea from observations:  
681 long-term surface changes, sub-surface and coastal responses, *Front. Mar. Sci.*, 9, 785771,  
682 <https://doi.org/10.3389/fmars.2022.785771>, 2022.
- 683 Kourafalou, V. H., and Barbopoulos, K.: High resolution simulations on the North Aegean Sea seasonal circulation, *Ann.  
684 Geophys.*, 21, 251–265, <https://doi.org/10.5194/angeo-21-251-2003>, 2003.



- 685 Laloyaux, P., de Boisseson, E., Balmaseda, M., Bidlot, J.-R., Broennimann, S., Buizza, R., et al.: CERA-20C: A coupled  
686 reanalysis of the twentieth century. *Journal of Advances in Modeling Earth Systems*, 10, 1172–1195,  
687 <https://doi.org/10.1029/2018MS001273>, 2018.
- 688 Lellouche, J.-M., Greiner, E., Romain, B., et al.: The Copernicus global 1/12° oceanic and sea ice GLORYS12 reanalysis,  
689 *Front. Earth Sci.*, 9, 698876, <https://doi.org/10.3389/feart.2021.698876>, 2021.
- 690 Lhotka, O., Bešťáková, Z., and Kyselý, J.: Prolongation of compound dry–hot seasons over Europe under climate change  
691 scenarios, *Earth’s Future*, 11, e2023EF003557, <https://doi.org/10.1029/2023EF003557>, 2023.
- 692 Lionello, P., and Scarascia, L.: The relation between climate change in the Mediterranean region and global warming, *Reg.*  
693 *Environ. Change*, 18, 1481–1493, <https://doi.org/10.1007/s10113-018-1290-1>, 2018.
- 694 Liu, C., Liang, X., and Yu, L.: Salinity trends and mass balances in the Mediterranean Sea: revisit the role of air–sea freshwater  
695 fluxes and oceanic exchange, *Ocean Sci.*, 21, 2069–2083, <https://doi.org/10.5194/os-21-2069-2025>, 2025.
- 696 Madec, G., and the NEMO Team: NEMO ocean engine – version 4.0, Institut Pierre-Simon Laplace (IPSL), France, 2017.
- 697 Marcos, M., and Tsimplis, M. N.: Coastal sea level trends in southern Europe, *Geophys. J. Int.*, 175, 70–82,  
698 <https://doi.org/10.1111/j.1365-246X.2008.03892.x>, 2008.
- 699 Margirier, F., Testor, P., Heslop, E., et al.: Abrupt warming and salinification of intermediate waters interplays with decline  
700 of deep convection in the northwestern Mediterranean Sea, *Sci. Rep.*, 10, 20923, [https://doi.org/10.1038/s41598-020-77859-](https://doi.org/10.1038/s41598-020-77859-5)  
701 5, 2020.
- 702 MedECC: Climate and Environmental Change in the Mediterranean Basin – Current Situation and Risks for the Future, First  
703 Mediterranean Assessment Report, Union for the Mediterranean, Plan Bleu, UNEP/MAP, Marseille, France, 632 pp.,  
704 <https://doi.org/10.5281/zenodo.4768833>, 2020.
- 705 Morel, A., and Maritorena, S.: Bio-optical properties of oceanic waters: a reappraisal, *J. Geophys. Res.-Oceans*, 106, 7163–  
706 7180, <https://doi.org/10.1029/2000JC000319>, 2001.
- 707 Nakanishi, M., and Niino, H.: An improved Mellor–Yamada level-3 model: its numerical stability and application to a regional  
708 prediction of advection fog, *Bound.-Lay. Meteorol.*, 119, 397–407, <https://doi.org/10.1007/s10546-005-9030-8>, 2006.
- 709 Pinardi, N., and Masetti, E.: Variability of the large scale general circulation of the Mediterranean Sea from observations and  
710 modelling: A review. *Palaeogeogr. Palaeoclimatol. Palaeoecol.*, 158, 153–173, [https://doi.org/10.1016/S0031-0182\(00\)00048-](https://doi.org/10.1016/S0031-0182(00)00048-1)  
711 1, 2000.
- 712 Pisano, A., et al.: New high-resolution Mediterranean SST reanalysis products from the Copernicus Marine Environment  
713 Monitoring Service, *Remote Sens. Environ.*, 243, 111781, <https://doi.org/10.1016/j.rse.2020.111781>, 2020.
- 714 Pisano, A., Marullo, S., Artale, V., et al.: New evidence of Mediterranean climate change and variability from sea surface  
715 temperature observations, *Remote Sens.*, 12, 132, <https://doi.org/10.3390/rs12010132>, 2020.
- 716 Pujol, M.-I., Dupuy, S., Vergara, O., et al.: Refining the resolution of DUACS along-track Level-3 sea level altimetry products,  
717 *Remote Sens.*, 15, 793, <https://doi.org/10.3390/rs15030793>, 2023.



- 718 Ridal, M., Bazile, E., Le Moigne, P., et al.: CERRA, the Copernicus European Regional Reanalysis system, *Q. J. Roy. Meteor.*  
719 *Soc.*, 150, 3385–3411, <https://doi.org/10.1002/qj.4764>, 2024.
- 720 Ruti, P. M., et al.: Med-CORDEX Initiative for Mediterranean climate studies, *Bull. Amer. Meteor. Soc.*, 97, 1187–1208,  
721 <https://doi.org/10.1175/BAMS-D-14-00176.1>, 2016.
- 722 Sammartino, M., Aronica, S., Santoleri, R., and Buongiorno Nardelli, B.: Retrieving Mediterranean Sea Surface Salinity  
723 Distribution and Interannual Trends from Multi-Sensor Satellite and In Situ Data. *Remote Sensing*, 14(10), 2502,  
724 <https://doi.org/10.3390/rs14102502>, 2022.
- 725 Senatore, A., Davolio, S., Furnari, L., and Mendicino, G.: Reconstructing flood events in Mediterranean coastal areas using  
726 different reanalyses and high-resolution meteorological models, *J. Hydrometeorol.*, 21, 1865–1887,  
727 <https://doi.org/10.1175/JHM-D-19-0270.1>, 2020.
- 728 Skamarock, W. C., Klemp, J. B., Duda, M. G., et al.: A description of the Advanced Research WRF model version 4.3.3,  
729 NCAR Tech. Note, <https://doi.org/10.5065/1dfh-6p97>, 2021.
- 730 Skliris, N., Zika, J. D., Herold, L., et al.: Mediterranean Sea water budget long-term trend inferred from salinity observations,  
731 *Clim. Dyn.*, 51, 2857–2876, <https://doi.org/10.1007/s00382-017-4053-7>, 2018.
- 732 Soukissian, T. H., Karathanasi, F., and Axaopoulos, P.: Offshore renewable energy in the Mediterranean Sea: a review of the  
733 resource, existing projects and prospects, *Renew. Energy*, 179, 1225–1241, <https://doi.org/10.1016/j.renene.2021.07.109>,  
734 2021.
- 735 Storto, A., Dobricic, S., Masina, S., and Di Pietro, P.: Assimilating along-track altimetric observations through local  
736 hydrostatic adjustment in a global ocean variational assimilation system, *Mon. Weather Rev.*, 139, 738–754,  
737 <https://doi.org/10.1175/2010MWR3350.1>, 2011.
- 738 Storto, A.: Variational quality control of hydrographic profile data with non-Gaussian errors for global ocean variational data  
739 assimilation systems, *Ocean Model.*, 104, 226–241, <https://doi.org/10.1016/j.ocemod.2016.06.011>, 2016.
- 740 Storto, A., Oddo, P., Cipollone, A., Mirouze, I., and Lemieux-Dudon, B.: Extending an oceanographic variational scheme to  
741 allow for affordable hybrid and four-dimensional data assimilation, *Ocean Model.*, 128, 67–86,  
742 <https://doi.org/10.1016/j.ocemod.2018.06.005>, 2018.
- 743 Storto, A., Alvera-Azcárate, A., Balmaseda, M. A., et al.: Ocean reanalyses: recent advances and unsolved challenges, *Front.*  
744 *Mar. Sci.*, 6, 418, <https://doi.org/10.3389/fmars.2019.00418>, 2019a.
- 745 Storto, A., Masina, S., Simoncelli, S., et al.: The added value of the multi-system spread information for ocean heat content  
746 and steric sea level investigations in the CMEMS GREP ensemble reanalysis product, *Clim. Dyn.*, 53, 287–312,  
747 <https://doi.org/10.1007/s00382-018-4585-5>, 2019b.
- 748 Storto, A., Hesham Essa, Y., de Toma, V., Anav, A., Sannino, G., Santoleri, R., and Yang, C.: MESMAR v1: a new regional  
749 coupled climate model for downscaling, predictability, and data assimilation studies in the Mediterranean region, *Geosci.*  
750 *Model Dev.*, 16, 4811–4833, <https://doi.org/10.5194/gmd-16-4811-2023>, 2023.
- 751 Storto, A., and Yang, C.: Acceleration of the ocean warming from 1961 to 2022 unveiled by large-ensemble reanalyses, *Nat.*  
752 *Commun.*, 15, 545, <https://doi.org/10.1038/s41467-024-44749-7>, 2024.



- 753 Storto, A., Chierici, G., Pfeffer, J., Barnoud, A., Bourdalle-Badie, R., Blazquez, A., Cavaliere, D., Lalau, N., Coupry, B.,  
754 Drevillon, M., Fourest, S., Larnicol, G., and Yang, C.: Variability in manometric sea level from reanalyses and observation-  
755 based products over the Arctic and North Atlantic oceans and the Mediterranean Sea, in: 8th edition of the Copernicus Ocean  
756 State Report (OSR8), edited by: von Schuckmann, K., Moreira, L., Grégoire, M., Marcos, M., Staneva, J., Brasseur, P., Garric,  
757 G., Lionello, P., Karstensen, J., and Neukermans, G., Copernicus Publications, State Planet, 4-osr8, 12,  
758 <https://doi.org/10.5194/sp-4-osr8-12-2024>, 2024.
- 759 Storto, A., de Toma, V., and Yang, C.: MESMAR-R: A Coupled Regional Reanalysis for the Mediterranean Region Covering  
760 the period 1993-2024 [Data set]. Zenodo. <https://doi.org/10.5281/zenodo.17829847>, 2025.
- 761 Tootoonchi, R., Bordoni, S., and D'Agostino, R.: Revisiting the moisture budget of the Mediterranean region in the ERA5  
762 reanalysis, *Weather Clim. Dynam.*, 6, 245–263, <https://doi.org/10.5194/wcd-6-245-2025>, 2025.
- 763 van der Meer, M., de Roda Husman, S., and Lhermitte, S.: Deep learning regional climate model emulators: a comparison of  
764 two downscaling training frameworks, *J. Adv. Model. Earth Syst.*, 15, e2022MS003593,  
765 <https://doi.org/10.1029/2022MS003593>, 2023.
- 766 von Schuckmann, K., Storto, A., Simoncelli, S., Raj, R.P., Samuelsen, A., de Pascual Collar, A., Garcia Sotillo, M., Szerkely,  
767 T., Mayer, M., Peterson, K.A., et al.: Ocean heat content, in CMEMS ocean state report 2, *J. Oper. Oceanogr.* 11 (sup1), S1–  
768 S142, <https://doi.org/10.1080/1755876X.2018.1489208>, 2018.
- 769 von Schuckmann, K., Palmer, M., Trenberth, K., et al.: An imperative to monitor Earth's energy imbalance, *Nat. Clim. Change*,  
770 6, 138–144, <https://doi.org/10.1038/nclimate2876>, 2016.
- 771 Zittis, G., Bruggeman, A., and Lelieveld, J.: Revisiting future extreme precipitation trends in the Mediterranean, *Weather Clim.*  
772 *Extrem.*, 34, 100380, <https://doi.org/10.1016/j.wace.2021.100380>, 2021.
- 773 Zuo, H., Balmaseda, M. A., Tietsche, S., Mogensen, K., and Mayer, M.: The ECMWF operational ensemble reanalysis–  
774 analysis system for ocean and sea ice: a description of the system and assessment, *Ocean Sci.*, 15, 779–808,  
775 <https://doi.org/10.5194/os-15-779-2019>, 2019.